AFRL-RD-PS-
TP-2020-0016

MODULAR ANTENNAS FOR SMALL SATELLITES

Christos Christodoulou

University of New Mexico
Department of Electrical and Computer Engineering
Albuquerque, NM 87131

05 June 2018

Final Report

AIR FORCE RESEARCH LABORATORY
Directed Energy Directorate
3550 Aberdeen Ave SE
AIR FORCE MATERIEL COMMAND
KIRTLAND AIR FORCE BASE, NM 87117-5776

REPORT DOCUMENTATION PAGE

Form Approved
OMB No. 0704-0188

1. REPORT DATE *(DD-MM-YYYY)*	2. REPORT TYPE	3. DATES COVERED
05-06-2018	Final Report	24-03-2015 to 24-03-2018

4. TITLE AND SUBTITLE
Modular Antennas for Small Satellites

5a. CONTRACT NUMBER
FA9453-15-1-0300

5b. GRANT NUMBER

5c. PROGRAM ELEMENT NUMBER

6. AUTHOR(S)

Christos Christodoulou

5d. PROJECT NUMBER

5e. TASK NUMBER

5f. WORK UNIT NUMBER

7. PERFORMING ORGANIZATION NAME(S) AND ADDRESS(ES)
Department of Electrical and Computer Engineering
University of New Mexico
Albuquerque, NM 87131

8. PERFORMING ORGANIZATION REPORT NUMBER

9. SPONSORING / MONITORING AGENCY NAME(S) AND ADDRESS(ES)

Air Force Research Laboratory
3550 Aberdeen Ave, SE
Kirtland AFB, NM 87117-5776

10. SPONSOR/MONITOR'S ACRONYM(S)
AFRL/RDMX

11. SPONSOR/MONITOR'S REPORT NUMBER(S)
AFRL-RD-PS-TP-2020-0016

12. DISTRIBUTION / AVAILABILITY STATEMENT
Approved for public release; distribution is unlimited.

13. SUPPLEMENTARY NOTES
Public affairs release approval number: AFRL-2021-0212.

14. ABSTRACT
The objective of this research was to develop new concepts of "modular antennas" for small satellites. Antennas proposed for small satellites need to be packed during the launch phase and then deploy once in space. They need to exhibit circular polarization, an acceptable gain, a reasonable bandwidth and, a sufficient beam-width. A modular antenna allows for a wide range of applications such as adaptive beamsteering, remote sensing, radar, surveillance, and communications with other satellites or ground stations at various frequencies. Various antenna types that have been designed, fabricated and tested in this research effort include, helical antennas, conical antennas, reconfigurable antennas, wideband antennas, foldable antennas, antennas integrated with solar panels, and MIMO antennas. The presented antennas can be deployed on a cluster of small satellites that can increase possible future communication functionalities.

15. SUBJECT TERMS
Reconfigurable antennas, deployable, frequency reconfiguration, polarization reconfiguration, composite tape, antenna diversity design, log-spiral, conical antennas, inverted-F antenna, rectifying circuit, transparent antenna, rectenna.

16. SECURITY CLASSIFICATION OF:			17. LIMITATION OF ABSTRACT	18. NUMBER OF PAGES	19a. NAME OF RESPONSIBLE PERSON
a. REPORT	b. ABSTRACT	c. THIS PAGE			Eunsook Hwang
Unclassified	Unclassified	Unclassified	SAR	68	19b. TELEPHONE NUMBER *(include area code)*

Table of Contents

LIST OF FIGURES iv
1 SUMMARY 1
2 INTRODUCTION 1
3 ANTENNA STRUCTURES 2
3.1 Conical Log-Spiral Antenna 2
3.1.1 Comparison of Feeding Schemes 2
3.1.2 Balanced Input Feed 3
3.1.3 Assembly of Antenna and Feed 4
3.2 Antennas based on Bi-Stable Composite Tape Spring Materials 7
3.2.1 The Bi-Stable Composite Tape Spring Material 7
3.2.2 Deployable Dipole With bi-Stable Composite Tape Spring 9
3.2.3 CubeSat Antenna Concepts Using a Composite Tape Spring 9
3.3 Diversity Antenna Structures 13
3.3.1 Dual Antenna Element Integration 14
3.3.2 Eight Element Antenna Structure 16
3.3.3 Integration of a Printed Parasitic Reflector 18
1) Effect on the input reflection coefficient of any curved and straight dipole: 18
2) Effect on the isolation between the curved dipoles: 19
3) Effect on the gain pattern of the curved/straight dipoles: 19
4) Effect on the polarization of the curved/straight dipoles: 21
3.3.4 Assessment of the Fabricated Prototype 21
3.3.5 Diversity System Analysis 23
3.3.6 Control of the System's Radiating Elements 26
3.4 Integrating Antenna Arrays over Solar Cells for Dual Source of Energy Harvesting 31
3.4.1 Single Element Design 32
3.4.2 Array Implementation 35
3.4.3 Effect of Antenna Arrays on the Solar Panel 40
3.4.4 Rectifier Circuit Design 42
3.5 Ridge-fed Conical Horn Antenna 44
3.5.1 Antenna Fabrication & Measurement 49
3.5.2 Material Characterization 55

4 CONCLUSION 57
5 References 58
6 List of Symbols, Abbreviations, and Acronyms 61

LIST OF FIGURES

Figure 1. Top and bottom feeding for log-spiral 4
Figure 2. Input match for the two feeding arrangements 4
Figure 3. Polar cross section of far field patterns 5
Figure 4. Layout of Balun for balanced feeding 5
Figure 5. S-parameters of Balun 6
Figure 6. Phase between ports 2 and 3 6
Figure 7. SIMPLE boom shown in the a) partially deployed and b) fully deployed states [14, 15] 8
Figure 8. The cross section of the composite tape spring dipole with a expanded view of the central part". 8
Figure 9. The Dipole with the actual composite tape spring with a zoomed in view of its excitation 10
Figure 10. The Dipole with the rectangular shaped composite tape spring with a zoomed view of its excitation 10
Figure 11. The measurement setup 10
Figure 12. A comparison between the monopole's measured reflection coefficient and the dipole's simulated reflection coefficient showing great analogy 11
Figure 13. The deployed and stowed monopole with their respective lengths. 11
Figure 14. The Dipole Antenna's 3-D Radiation Pattern at 250 MHz 11
Figure 15. The three element copper based log periodic antenna array with its radiation pattern at 540 MHz at the E-plane cut. 12
Figure 16. The reflection coefficient of the three element log periodic antenna 12
Figure 17. The proposed Composite tape-spring log periodic crossed dipole antenna array concept 13
Figure 18. The curved dipole structure, (b) The straight dipole, (c) The reflection coefficient for both structures, (d) The balun circuitry. 14
Figure 19. (a) The integration of both radiating elements, (b) The reflection coefficient for the straight dipole, (c) and for the curved dipole. 15
Figure 20. (a) The change in the total gain pattern for the (a) straight dipole (dotted: 5 GHz/Solid: 4.8 GHz), (b) curved dipole (5.8 GHz) 16
Figure 21. The diversity antenna structure composed of eight radiating elements. 17
Figure 22. The simulated S-parameters between the various (a) straight dipoles, (b) curved dipoles. 18
Figure 23. The final antenna structure after the integration of the printed parasitic element (a) Top view, (b) Bottom view. 18
Figure 24. (a) The effect of the printed parasitic reflector on the reflection coefficient of both radiating structures, (b) The change in the isolation between C3 and C4 19
Figure 25. The total gain pattern after the addition of the printed parasitic element for (a) C3 and C4 (f=5.6 GHz), (b) S3 and S4 (f=4.8 GHz), (c) T3D gain pattern when C3 or C4 is activated (f=5.6 GHz) , (d) S1 or S2 is activated (f=4.8 GHz). 20
Figure 26. The gain difference between the cross-polarized component of S1/C1 and the co-polarized component of S4/C4. 20
Figure 27. The top and bottom layer of the fabricated prototype. 21

Figure 28. The reflection coefficient of any curved dipole and straight dipole. 21
Figure 29. The simulated (dotted line) and measured (solid line) total gain pattern in the *XZ* plane for S3 at *f*=4.8 GHz and C4 at *f*=5.6 GHz, (b) The measured gain for S1, S2, C3, and C4 in the *XY* plane.....22
Figure 30. The cumulative distribution function for the (a) four curved dipoles (random-LOS), (b) four straight dipoles (RIMP), (c) The TARC between S1 and S2 as well as C1 and C2 for various phase differences. 25
Figure 31. (a) The control of two different radiating elements via a reconfigurable feeding network, (b) The physical dimensions of the proposed reconfigurable feeding network.....26
Figure 32. The comparison between the simulated and measured S-parameters of the feeding network (a) when both diodes are OFF, (b) when D1 or D2 is ON.....27
Figure 33. (a)The bottom view of the integration of the four feeding networks underneath the curved printed reflector, (b) The location of the eight diodes within the four feeding networks, (c) The fabricated prototype, (d) The simulated and measured reflection coefficient.....28
Figure 34. The change in the measured gain pattern with and without the reconfigurable feeding network when feeding (a) C3, (b) S3.....29
Figure 35. The detailed dimensions of the antenna structure operating at (a) the upper band, (b) the lower band, (c) the fabricated prototypes for both structures. 33
Figure 36. The effect of the width of the extended ground plane on the antenna's (a) reflection coefficient, (b) gain pattern in the Φ= 0^o plane, (c) and 90^o plane. 34
Figure 37. The simulated and measured reflection coefficient for the inverted-F antenna placed (a) at the upper edge, (b) lower edge of the solar panel.....35
Figure 38. The physical array structure over a solar cell, (b) The fabricated array structure with the solar panel, (c) The feeding of the two array for scenario 3, (d) and scenario 4. 36
Figure 39. The change in the gain pattern at *f*=2.29 GHz for (a) Φ= 0^o, (b) Φ= 90^o, (c) The 3D gain pattern at *f*=1.87 GHz for the one element antenna, (d) The change in the 3D gain pattern for the two elements array (Elements 3 and 4). 36
Figure 40. (a) The simulated and measured reflection coefficient for elements 1 and 4 of the two arrays, (b) The measured isolation between elements 1 and 2 as well as elements 2 and 4. 37
Figure 41. (a) The measured reflection coefficient when only one element either array is fed (scenario 1 and 2), (b) The comparison between the simulated and measured reflection coefficient when each array is fed by a power splitter simultaneously (scenario 3). 38
Figure 42. (a) The reflection coefficient for the case when the four elements are fed by a four ways power splitter (scenario 4), (b) The corresponding simulation setup for scenario (4).....39
Figure 43. (a) The normalized array radiation pattern for Φ= 0^o (left) and Φ= 90^o (right) cut planes (a) for the first array at *f*=2.29 GHz, (b) and for the second array at *f*=1.87 GHz.....40
Figure 44. (a) The fabricated copper and transparent array structure with the solar panel, (b) The soldering setup of the transparent array elements where the conductive silver epoxy is apparent on the array ground plane.....41
Figure 45. The reflection coefficient for the transparent array when both arrays are fed simultaneously through two different power splitters (scenario 3). 42
Figure 46. (a) The structure of the voltage doubler rectifying circuit, (b) The corresponding fabricated prototype. 43
Figure 47. (a) The measured efficiency of the wideband rectifier circuit, (b) The rectification efficiency at the resonant frequency of the two arrays. 44
Figure 48. Concept: Ridge-fed conical horn antenna. 45

Figure 49. Reflection Coefficient Ridge-fed Conical Horn antenna. 45
Figure 50. Discretized gain plot of the Ridge-fed Conical Horn antenna compared with the gain of the Quad-ridged horn antenna. 46
Figure 51: Angular 3dB beam width of the Ridge-fed Conical Horn antenna com- pared with the Quad-ridged and plotted against frequency.....46
Figure 52: Axial Ratio in dB at boresight of the Ridge-fed Conical Horn antenna compared with the Quad-ridged and plotted against frequency. 47
Figure 53. (a) Radiation Pattern at 2GHz, 3GHz, and 4GHz. (b) Radiation Pattern at 5GHz, 6GHz, and 7GHz.....48
Figure 54. (a) Radiation Pattern at 8 GHz, 9 GHz, and 10 GHz. (b) Radiation Pattern at 11GHz, 12 GHz and 13 GHz.....48
Figure 55. Fabricated fin 49
Figure 56. (a)Feed slot milled on the fin side (b) Inserted coax which turns into a probe and feeds the ridge.....50
Figure 57. S-parameter measurement set up for the fabricated quad-ridge.....51
Figure 58. Γ comparison between measured and simulated for 50Ω. 52
Figure 59. (a) 2 GHz radiation pattern horizontal plane. (b) 2GHz radiation pattern vertical plane. 53
Figure 60. (a) 3GHz Horizontal radiation pattern. (b) 3GHz Vertical radiation pattern. 53
Figure 61. (a) 7 GHz Horizontal radiation pattern. (b) 7GHz Vertical radiation pattern.....54
Figure 62. (a)13GHz Horizontal radiation pattern. (b) 13GHz Vertical radiation pattern.....54
Figure 63: Material Description 55
Figure 64. (a) Substrate 1. (b) Substrate 2.....56
Figure 65. (a) Substrate 3. (b) Substrate 4.....56
Figure 66. (a) Substrate 5. (b) Substrate 6. 56

1 SUMMARY

The main focus of this work was the design and analysis of novel space antenna concepts for cubesats that cover different frequency ranges and applications. The main theme in all antennas designed was based on the "modular antenna concept" that allows for a wide range of applications such as adaptive beamsteering, remote sensing, radar, surveillance, and communications with other satellites or ground stations at various frequencies. Various antenna types that have been designed, fabricated and tested in this research effort include, helical antennas, conical antennas, reconfigurable antennas, wideband antennas, foldable antennas, antennas integrated with solar panels, and MIMO antennas. The presented antennas can be deployed on a cluster of small satellites that can increase possible future communication functionalities.

2 INTRODUCTION

The low cost and quick turn around time of small satellites has revolutionized the satellite industry and space research. Small satellites are now a popular choice in space communication platforms and various other applications from telemetry and tracking to space weather monitoring. Government organizations, universities, and companies have developed various designs and deployment of small satellites with greater functionalities.

The one drawback in small satellites is their size restrictions on the design of multifunctional and high gain antennas. The design of deployable antenna structures, for example, is especially challenging at low frequencies such as UHF. Antennas need to fit and be stored inside the launch vehicle shroud during the trip to earth-orbit and then deploy once in space.

The operational frequency determines the microwave components and the digital processing system. Depending on the mission characteristics the satellite may have one or multiple antennas to cater to the satellite and the load which might require faster data rates for it's applications.

The preferred antenna choice for a CubeSat platform has been monopoles/dipoles or an array of wire antennas. Such antennas can be arranged in a manner to achieve circular polarization and a high gain. The omnidirectional properties of dipoles antennas as well as their natural linear polarization limit their required directivity and pointing control. Although dipoles are very popular, they don't represent the optimal antenna solutions for small satellite deployment. Their narrowband, low gain and low efficiency constitute major drawbacks [1-2]. Different antenna types are required to cater for the needs of small satellite communication such as patch antennas and, deployable hemispherical helical antennas [3,4]. Some researchers have also proposed active antennas for their CubeSat development [5]. Deployable parabolic reflector antennas have also been used for deployment over small and large satellites. However, the packing and deployment techniques of these types have to be optimized due to their large size.

Helical antennas have also been used on CubeSat antennas due to their natural circular polarization and wide bandwidth [6-7]. Patch antennas printed on CubeSat sides were also suggested as potential candidates for use on small satellites [8].

The purpose of this work was to design and develop antennas that are modular but also valid candidates for deployment over small satellites such as CubeSats. The antennas presented here cover a wide variety of applications. There are 5 main antenna structures that are discussed here.

The first model is based on a conical log-spiral antenna that has been designed to include a new type of feeding approach to direct the radiated energy away from the cubesat structure and fold the entire antenna and its feeding mechanism.

The second model is based on using specially made materials that can be folded and unfolded many times and take various shapes. The material can be mechanically flexible but also conductive in nature so it can be used as an antenna material. Examples on how log-periodic antennas can be constructed using this specific material are shown and discussed.

The third model is based on array antennas as a MIMO structure that helps in enhancing communications on cubesats. A fabricated model based on an 8 element diversity antenna system is shown and the entire array is thoroughly evaluated.

The fourth model emphasizes the integration of copper or transparent antennas with solar panels for multiple source harvesting mechanisms on a cubesat. This approach can allow the powering of any cubesat in space using space power beaming.

The last antenna structure is based on the integration of a ridge-fed conical horn that can be folded using new materials made that are very thin and mechanically flexible.

3 ANTENNA STRUCTURES

3.1 Conical Log-Spiral Antenna

The first antenna to presented here is a conical log-spiral antenna integrated with a new feeding scheme. This antenna is proposed for deployment on a CubeSat platform. The developed feeding technique allows for easier antenna deployment. A microstrip balun is also presented to provide the antenna with proper phase balance and impedance associated with the needed differential feed.

3.1.1 Comparison of Feeding Schemes

The conical log-spiral antenna has a radiation pattern that is directed towards the vertex of the cone. This is explained due to the slow to fast wave nature of the non-active to active regions of the spiral arms, respectively [9]. This transition leads to a backfire radiated pattern towards

the conical vertex. Feeding the conical log-spiral from the bottom of the antenna structure should lead the radiation pattern to fire away from the vertex of the cone by the change of active and non-active regions. As the desired direction of radiation is away from the CubeSat, a deployable ground plane is needed for a bottom feed setup

To have a performance comparison between the feeding mechanism for the top and bottom schemes, the antenna is first constructed within CST Microwave Studio as seen in Figure 1. The size of the ground plane is optimized for the bottom feeding scheme, where it is determined to be approximately the height of the antenna. The chosen frequency range of 2 GHz to 3.44 GHz is higher than the initial UHF design [10]; however, the frequency scaling reduces the size and cost of building the antenna

Comparing the input match of a 200Ω differential port, the reflection coefficient, shown in Figure 2, is better than -10dB across the band of interest. Figure 3 shows a polar cross section of the 3D radiated far field pattern of the two feeding configurations at lower (2 GHz) and upper (3.44 GHz) band edges. At the lower frequency the pattern remains similar, with the exception of the increased back lobe of 0dBi. The upper band edge has a higher directivity of 11dBi and a smaller half power beam width (HPBW), which is reduced from 90º to 50º. Investigating the electric field along the log-spiral, it can be seen that the beam width is reduced by the introduction of the ground plane. Since the ground plane is larger in wavelength at the upper band edge compared to the lower band edge, a larger effect on the higher frequency components is realized. These initial results show that the conical log-spiral can be excited from the lower part of the antenna structure and achieve similar attributes with minimal changes to the initial configuration

3.1.2 Balanced Input Feed

Like all antennas that need differential feeds, the input must be balanced to achieve the specified input match and radiation characteristics. For the log-spiral, it must be noted that any deformation of the radiation pattern can be traced back to balance of the input feed [11]. To solve this problem, a modified wideband microstrip balun is presented in this work, as shown in Figure 4. The concept is taken from a rat race 180º hybrid, which is broken down into a marchland balun and an in-phase power divider [5]. Port 1 is the input, port 2 and 3 are the outputs to be connected to the antenna arms, and port 4 is loaded with 50Ω to ground. Port 2 and 3 are approximately 3dB down and 180º out of phase with each other throughout the bandwidth. The S-parameters of the balun are shown in Figure 5. Since this structure's length is based on the center frequency, the phase balance between the two output ports may not remain constant, yet this balun design has shown that the phase remains at 180º ± 2º between the two output ports, as seen in Figure 6.

3.1.3 Assembly of Antenna and Feed

Ports 2 and 3 of the balun are connected to Micro-Coax 100Ω lines that are used as launches from the balun to the arms of the log-spiral. Within the deployment model, the balun shares the same ground plane as the antenna structure.

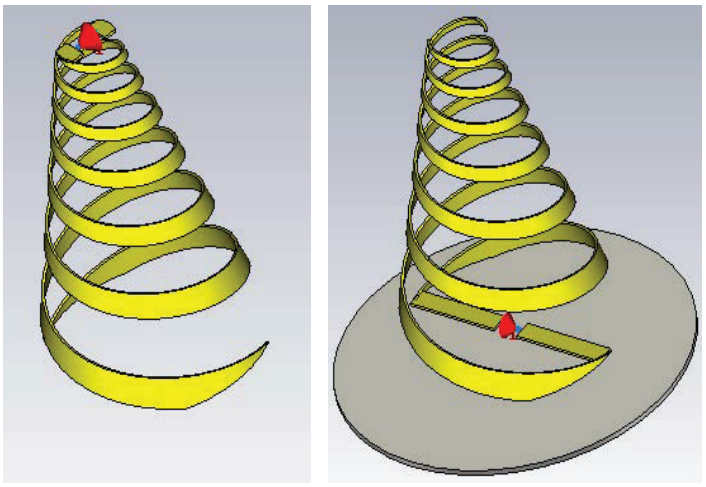

Figure 1. Top and bottom feeding for log-spiral

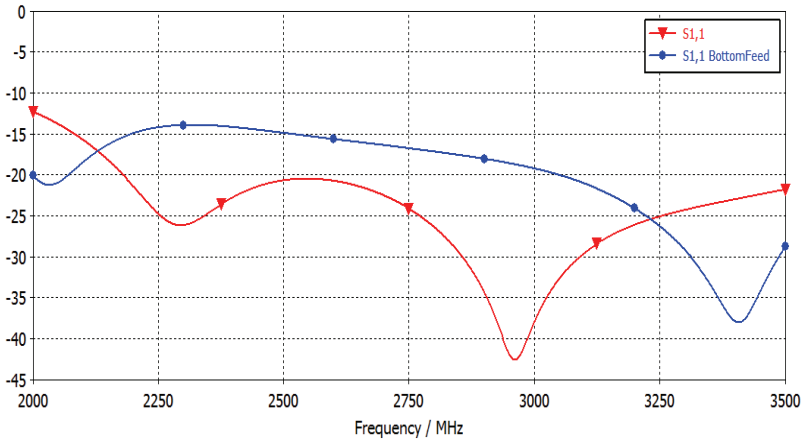

Figure 2. Input match for the two feeding arrangements

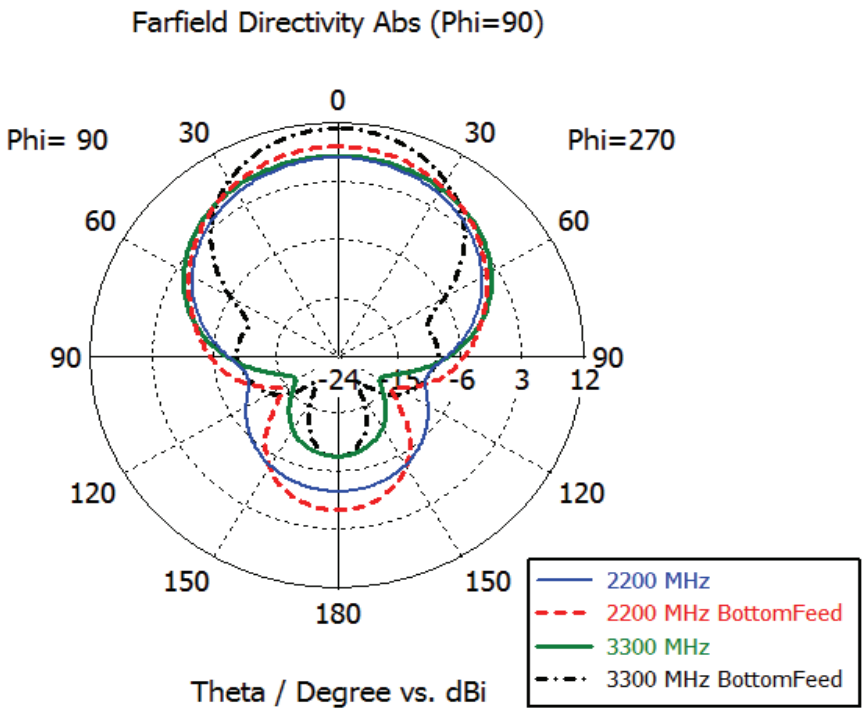

Figure 3. Polar cross section of far field patterns

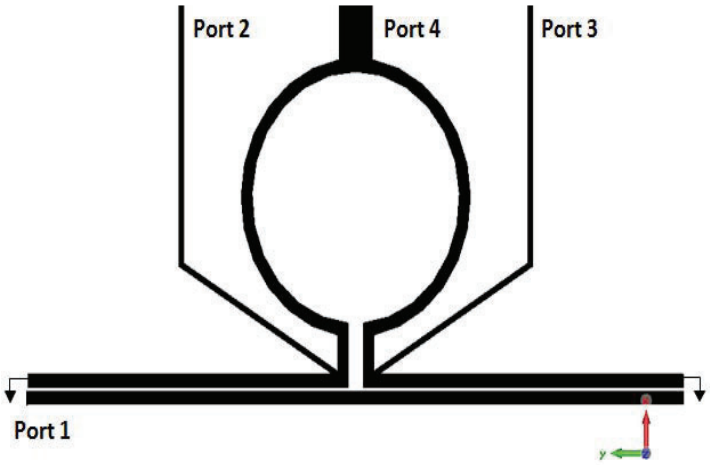

Figure 4. Layout of Balun for balanced feeding

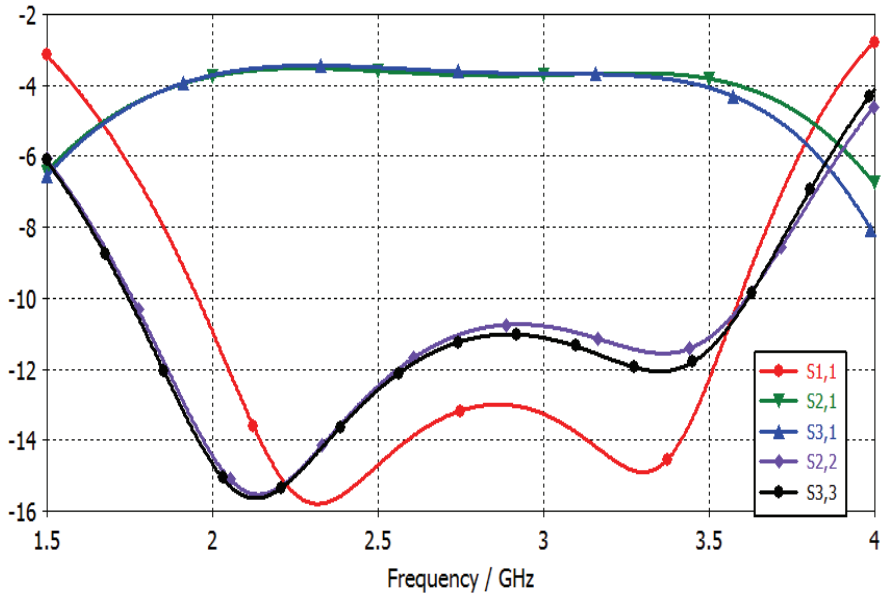

Figure 5. S-parameters of Balun

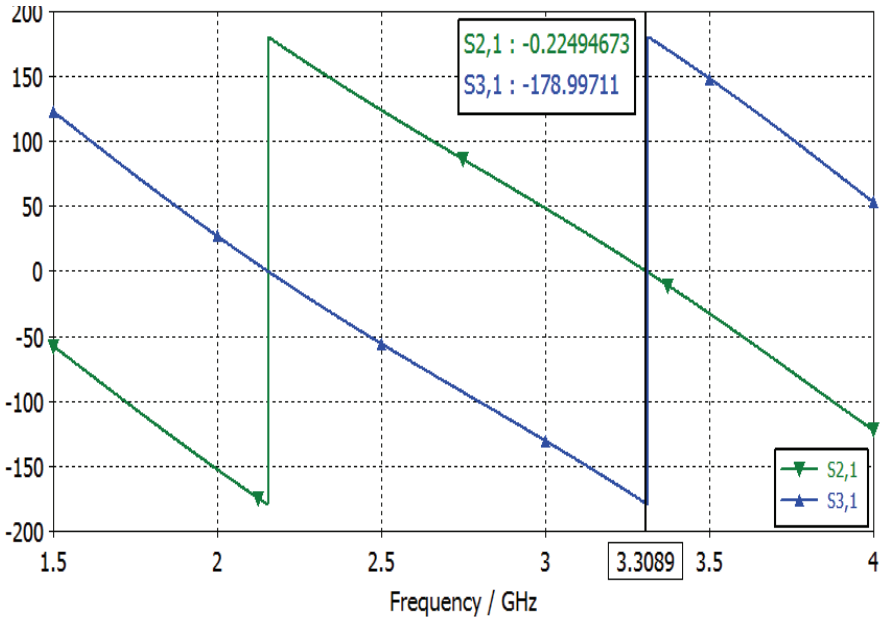

Figure 6. Phase between ports 2 and 3

3.2 Antennas based on Bi-Stable Composite Tape Spring Materials

A novel composite tape-spring that is suitable for use as a structural element of deployable space structures is introduced by Murphey [12,13]. The tape-spring has the unique property that it is neutrally stable. It is static in a continuum of positions without external forces to hold it. This class of structure is referred to as a Neutrally Elastic Mechanism (NEM) because its behavior is functionally equivalent to typical sliding contact joint mechanisms. A consequence of this neutral stability is that diminishingly small forces are required to roll or unroll the tape-spring. According to Murphey [12,13], such actuated NEM tape-springs offer four prominent features for deployable space structures. First, they allow controlled deployment, second, they allow controlled retraction, third, their neutral stability allows for zero stiffness isolators and actuators and finally, they allow mass efficient (with respect to stiffness and strength) structures in the fully deployed configuration.

Antenna design and structural engineering are two disciplines that typically don't merge until late in the antenna design process. Initial antenna design is completed with little regard for structural requirements and constraints; at the same time structural designs are made with little attention to their effects on antenna performance. In this particular type of antenna work these two tracks are merged from the beginning to leverage structural-electrical interactions for higher antenna performance and structural efficiency.

Thomas Murphey of the Air Force Research Laboratory Space Vehicles Directorate and Adam Biskner of LoadPath Inc., invented and developed a bi-stable glass composite tape spring with an embedded conductor to be used as a deployable antenna element [14]. This structural element is the basis for the CubeSat communication antenna proposed and tested in this letter which constitutes the first measured antenna designed with bi-stable composite tape springs.

3.2.1 The Bi-Stable Composite Tape Spring Material

The composite tape-spring presented herein is a curved bi-stable composite that rolls and unrolls. The composite is stable in both its deployed and stowed states. Unlike the neutrally stable tape spring, the bi-stable version has only two elastically stable physical states, fully rolled and fully extended. The intermediate state can be held stationary but not without an external force. The benefit of these structures is that they possess deployment authority yet do not bloom during deployment. Therefore physical reconfigurability (rolling and unrolling) can be accomplished with a one-way linear or rotary actuator unlike NEM tape springs that require two-way actuators. A deployable structure concept that utilizes bi-stable tape spring elements is presented in [14, 15] and shown in Figure 7.

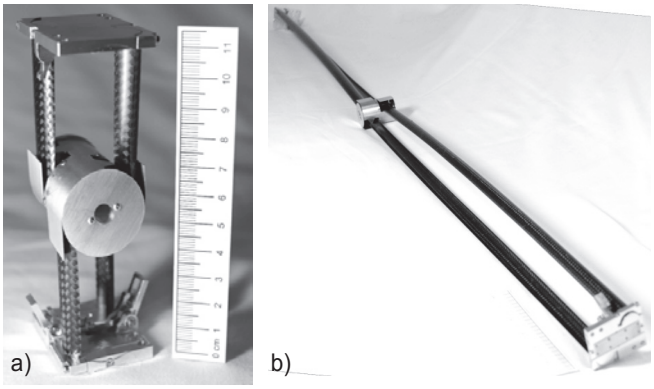

Figure 7. SIMPLE boom shown in the a) partially deployed and b) fully deployed states [14, 15]

An expanded cross section of the composite structure is shown in Figure 8. It is composed of three plies. The top and bottom are composed of a 45 degree biased Astroquartz fabric impregnated with toughened epoxy. Both layers have an arc length of 0.5 inches.

The relative electric permittivity is assumed to be 3.7 [16] at any frequency between 250 MHz and 500 MHz. The relative permeability is assumed to be equal to 1 and the loss tangent is assumed to be 0.0001. The middle layer is a 0.25 inch wide strip of copper alloy. Next to the copper is an epoxy filler. Astroquartz is used for its high strain to failure and low electrical conductivity characteristics. The copper alloy is used as a compromise between high strain to failure and high electrical conductivity.

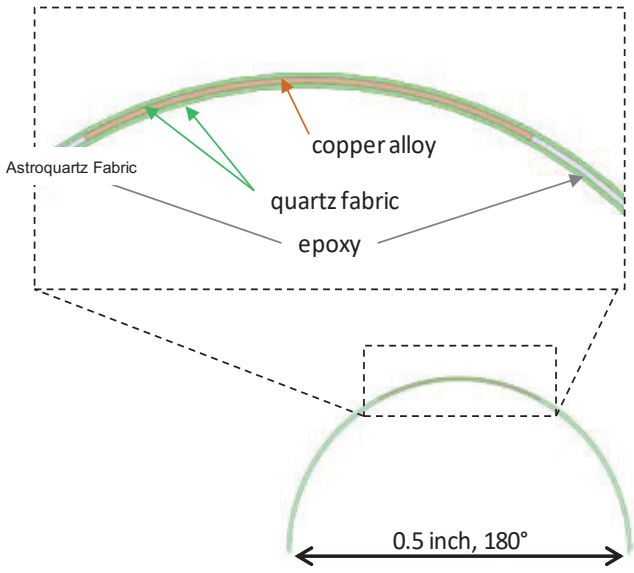

Figure 8. The cross section of the composite tape spring dipole with a expanded view of the central part".

3.2.2 Deployable Dipole With bi-Stable Composite Tape Spring

Using the bi-stable composite tape spring we design a dipole to operate at 250 MHz. To reduce processing time, the material is assumed to be of rectangular shape and not curved. We also assume the beryllium copper embedded in the middle has a width of 0.25 inches. The total width of each dipole arm is 0.5 inches. After calculations and simulations using Ansys' HFSS, the total dipole length is found to be equal to 22 inches which is equivalent to 0.465λ at 250 MHz. A zoomed-in view of the curved antenna with the actual material is shown in Figure 9 while the simulated dipole with the approximated tape spring is shown in Figure 10 with a zoomed-in view of its excitation.

The measurement of this dipole is done by using the image method [17]. A composite tape spring quarter wavelength monopole 11 inches long is measured on top of a large ground plane (45 inch x 60 inch) as shown in Figure 11. Figure 12 shows the average measured reflection coefficient compared to the dipole's simulated reflection coefficient. The antenna was rolled and unrolled about ten times and the reflection coefficient measured each time with no significant changes, proving that the antenna function is preserved through mechanical cycles. Figure 13 shows a picture of the deployed and stowed monopoles on top of the ground plane. Measurement results of the monopole verify the simulation approach and the feasibility of using this composite tape spring structure for antenna design. The simulated three-dimensional radiation pattern at 250 MHz is shown in Figure 14.

3.2.3 CubeSat Antenna Concepts Using a Composite Tape Spring

A copper based three element log periodic dipole antenna array with curved edges, shown in Figure 15, operates between 375 MHz and 540 MHz as shown in Figure 16. The three elements have lengths of 8.05 in, 6.5 in, and 4.78 in, respectively. The radiation pattern of this antenna array shown in Figure 15 is directed away from small element. These properties indicate this antenna is a good candidate as a CubeSat deployable antenna.

Based on all the previously discussed results, a 10 element log periodic crossed dipole array antenna was designed with the bi-stable composite tape spring proposed in the previous sections. With 10 elements this antenna can achieve at least 5dB gain and a frequency band of operation between 250 and 500 MHz. In addition to these constraints the radiation pattern of the proposed antenna is directive away from the small element where the directivity of this array antenna is determined by the log periodicity of the elements [17]. This antenna concept is shown in Figure 17.

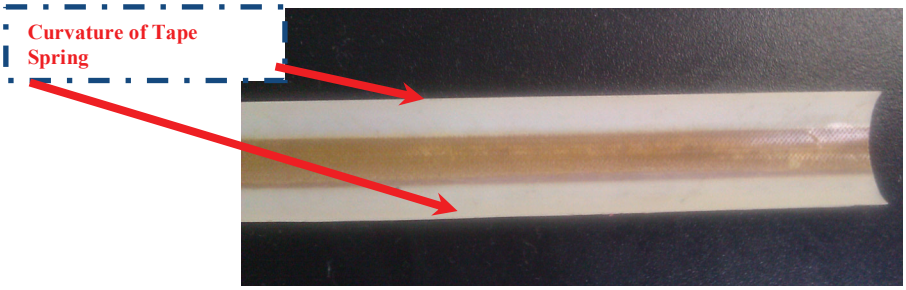

Figure 9. The Dipole with the actual composite tape spring with a zoomed in view of its excitation

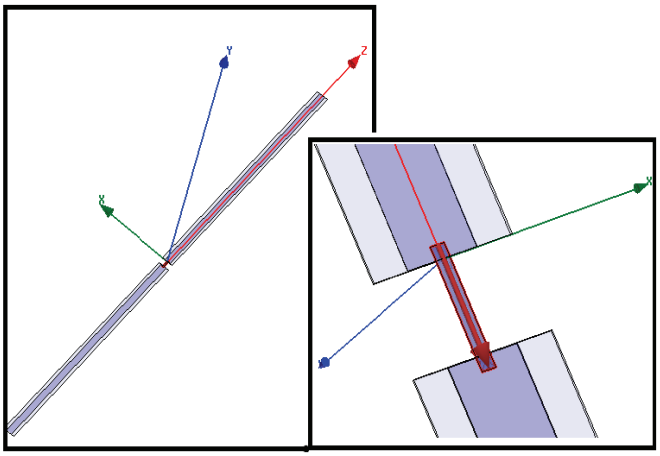

Figure 10. The Dipole with the rectangular shaped composite tape spring with a zoomed view of its excitation

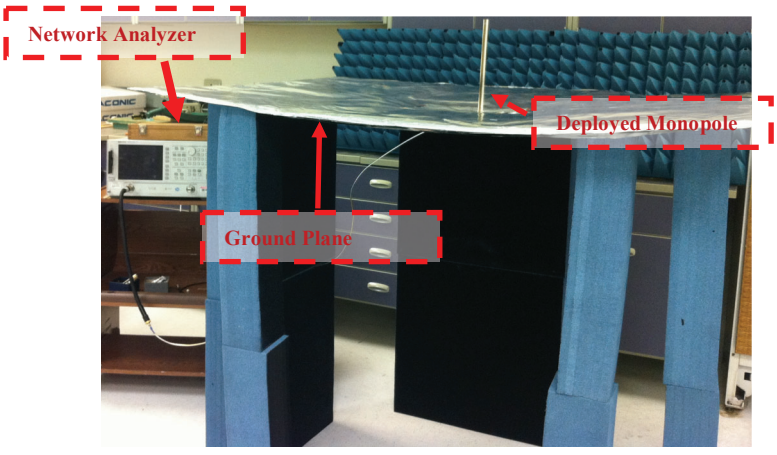

Figure 11. The measurement setup

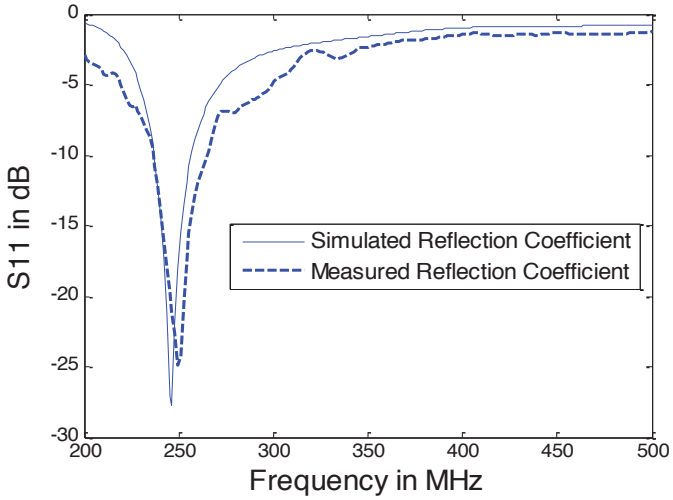

Figure 12. A comparison between the monopole's measured reflection coefficient and the dipole's simulated reflection coefficient showing great analogy

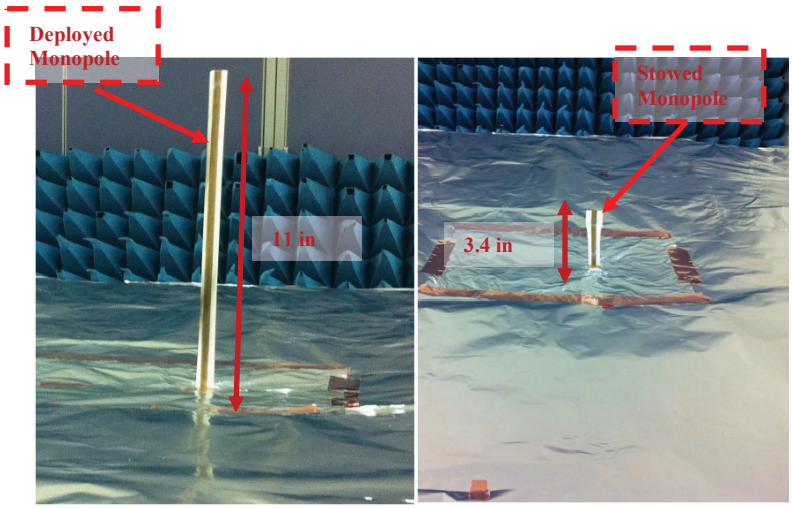

Figure 13. The deployed and stowed monopole with their respective lengths.

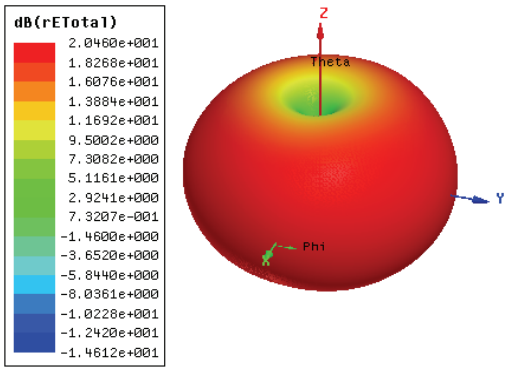

Figure 14. The Dipole Antenna's 3-D Radiation Pattern at 250 MHz

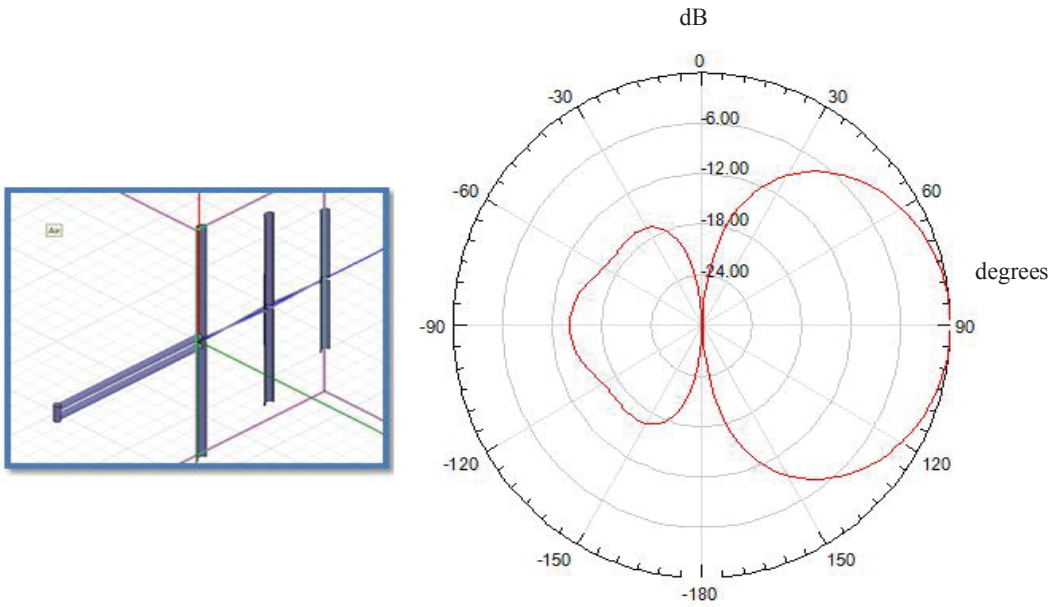

Figure 15. The three element copper based log periodic antenna array with its radiation pattern at 540 MHz at the E-plane cut.

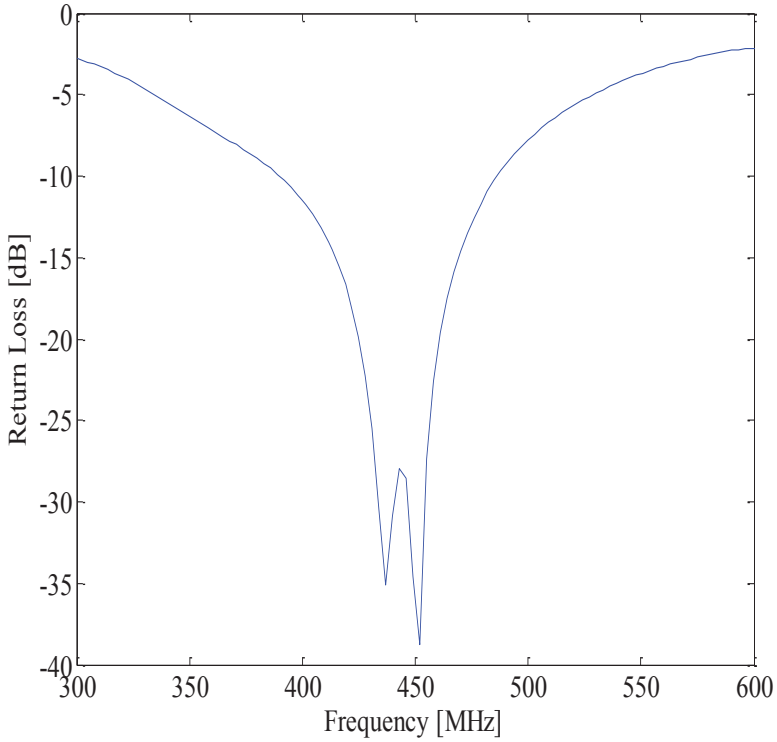

Figure 16. The reflection coefficient of the three element log periodic antenna

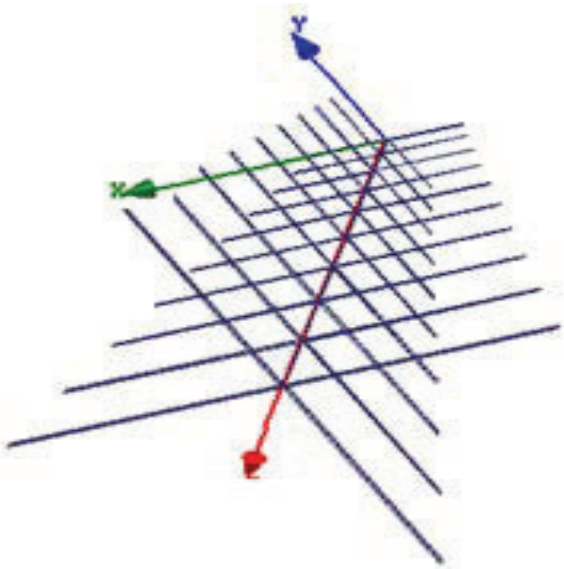

Figure 17. The proposed Composite tape-spring log periodic crossed dipole antenna array concept

The presented antennas exhibit good bandwidth, circular polarization and a satisfactory gain. The proposed bi-stable glass composite tape spring with imbedded copper alloy conductive element introduces new possible antenna configurations for CubeSats. This merging of structural engineering with the antenna design yielded a robust deployable antenna design.

3.3 Diversity Antenna Structures

Diversity antenna structures are required for next generation wireless systems to provide high data rates and increased channel capacity. Several antenna concepts have been presented in the literature with diversity behavior [18-28].

In this section, the design of a radiating system that is composed of two diversity antenna structures is presented [29,30]. Each diversity antenna structure is composed of four elements that operate over a different span of frequencies with a directive gain pattern. Two elements are aligned along the *x*-axis while the others two are placed along the *y*-axis to provide orthogonal polarization between the various radiating elements. A set of four curved dipoles constitute the first diversity structure while the second diversity structure is composed of four straight dipoles. The novelty of the presented work is based on the compact integration of the two antenna structures. Each structure is appropriately designed to actively shape the gain pattern of the other structure while at the same time enhancing the isolation levels. The novelty of this work is also focused on the simple feeding of the different dipoles through the integration of a multilayer surface mount chip balun in addition to the incorporation of a printed parasitic reflective surface in the empty space between the dipoles. Such integration contributes to the compactness of the design and enhances the isolation as well as the directive characteristics of the whole antenna system. The novelty of the work can also be assessed by the selective activation of each diversity antenna structure. Four reconfigurable feeding networks are placed

underneath the antenna's bottom layer and orthogonally to the printed curved reflector. Such selectivity enables the entire antenna diversity system to reconfigure its operating frequency.

3.3.1 Dual Antenna Element Integration

The design process of the complete antenna system is initiated by integrating two antenna elements in close proximity to each other. The two antennas are composed of a straight and curved dipoles. The purpose of such integration is to investigate the ability of one antenna structure, when inactive, to act as a prasitic reflector to the other active antenna. Figure 18a shows the structure of the curved dipole printed on top of Rogers 5880 substrate with a dielectric constant of 2.2 and a thickness of 1.6 mm. The length of the dipole (65.4 mm) corresponds to almost $3\lambda_g/2$ at f=5.8 GHz. The width of each dipole arm is designed to be 3.279 mm for a differential input impedance of 50 Ω. The structure of the straight dipole is shown in Figure 18bThis structure has a length of 23.325 mm and a width of 1.2 mm in order to operate at 5 GHz with a differential input impedance of 50 Ω. The straight dipole resonates at almost $\lambda_g/2$. The reflection coefficients for both radiating structures are summarized in Fugure 18c displaying the antennas' respective frequencies of operation. The excitation mechanism of both elements is highlighted in Figure 18d.

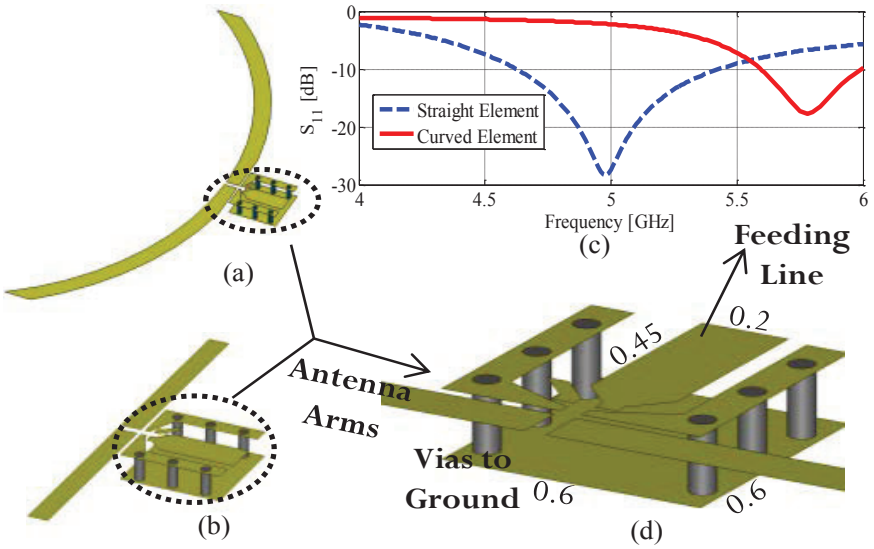

Figure 18. The curved dipole structure, (b) The straight dipole, (c) The reflection coefficient for both structures, (d) The balun circuitry.

A six-pin surface mount multilayer chip balun is used to feed the two arms of each dipole [31]. The balun provides the appropriate transition from the dipole's balanced structure to the unbalanced antenna feeding point by providing a phase difference of 180^0 between the two arms of each dipole. It also allows the appropriate transformation from an input impedance of 50 Ω to a differential impedance of 50 Ω between the dipole arms. Two pins of the integrated balun are connected to the two arms of the dipoles. Two other pins are connected to the

balun's ground through six vias. The ground has a dimension of 0.6 cm x 0.6 cm. One pin is connected to the antenna's SMA connector through the feeding line that has a length of 0.45 cm and a width of 0.2 cm.

The two dipole structures are then integrated together as shown in Figure 19 aon the same antenna substrate with a total dimension of 7.5 cm x 3.5 cm. The distance of separation *d* between the two radiating elements is optimized for a minimum effect on their matching and gain charactertistics. The presence of the curved dipole has an inductive effect on the input impedance of the straight dipole. Without the presence of the curved dipole, the reactive component of the input impedance of the straight dipole is -*j*0.37 Ω at 5 GHz. However, after the integration (*d*=0.8 cm), the reactive part changes to +*j*21.725 Ω at 5 GHz. This change forces the straight dipole to shift its resonant frequency to 4.8 GHz while maintaining the same physical length. The reflection coefficient of the straight dipole is shown in Figure 19b for different values of *d*. The best matching is obtained when *d* = 0.8 cm with an operation that shifts from 5 GHz to 4.8 GHz.

The effect of the straight dipole on the reflection coefficient of the curved element is negligible as shown in Figure 19c for different values of *d*. It is clear that the curved dipole preserves almost the same reflection coeffecient. This is related to the fact that the straight dipole is shorter in length and its parasitic effect is not noticeable on the curved dipole's input impedance. For the remainder of this work, the distance *d*=0.8 cm is kept between the two dipoles.

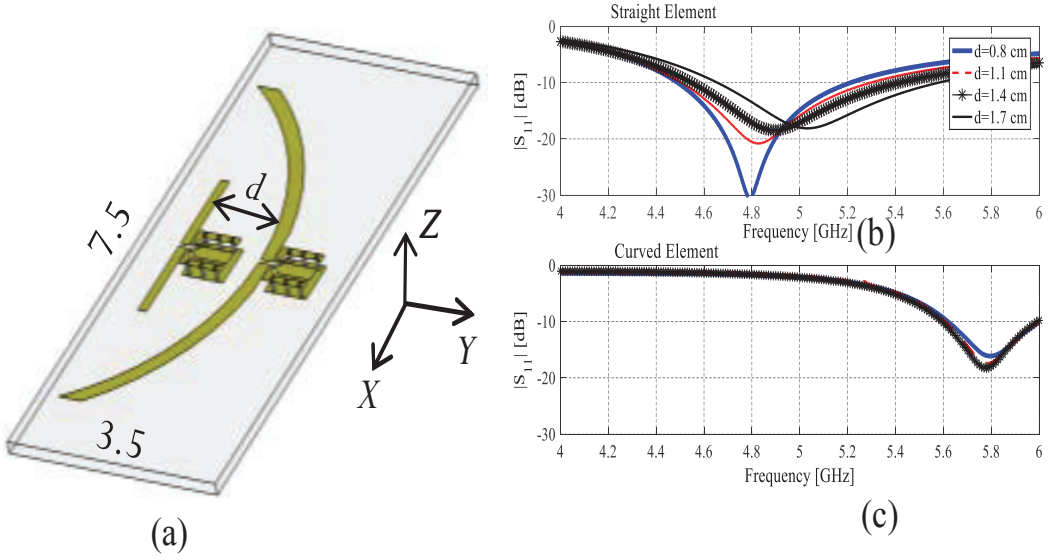

Figure 19. (a) The integration of both radiating elements, (b) The reflection coefficient for the straight dipole, (c) and for the curved dipole.

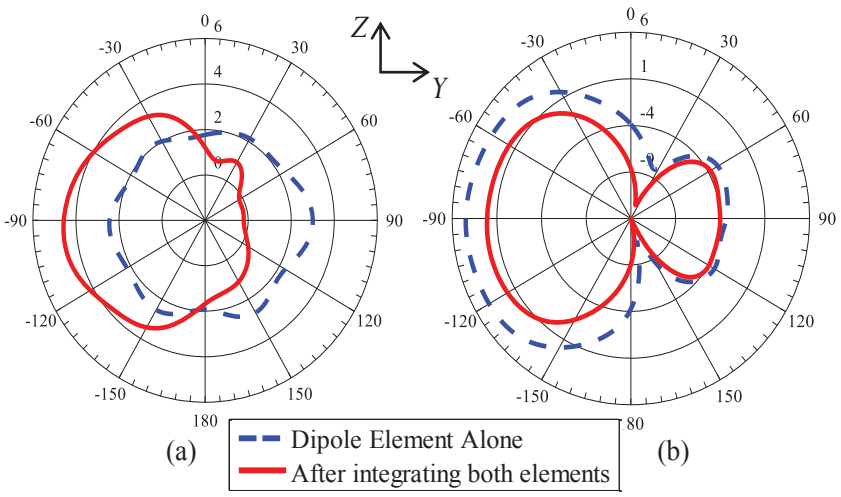

Figure 20. (a) The change in the total gain pattern for the (a) straight dipole (dotted: 5 GHz/Solid: 4.8 GHz), (b) curved dipole (5.8 GHz).

The change in the total gain pattern of the straight dipole antenna in the *YZ* plane is highlighted in Figure 20a. The pattern changes from omnidirectional to a directive one. The curved dipole element forces the radiated fields by the straight dipole to be directed towards one direction (-*y* direction) and blocks the radiation from the opposite direction (+*y* direction). The maximum total gain increases from 2.9 dBi at *f*=5 GHz (standalone) to 4.5 dBi at *f*=4.8 GHz (dual). As for the back lobe gain (at θ=90^o), its value drops from 2.9 dBi to -0.2 dBi.

The curved dipole by itself produces a directional pattern with a maximum realized gain of 4.45 dBi and a front to back gain ratio of 8.18 dBi. The parasitic effect of the straight dipole on the total gain pattern of the curved element is shown in Figure 20b. Such effect is noticed by a drop of almost 2 dB in the maximum realized gain as well as in the front to back gain ratio. Such drop is obtained since the close proximity of the straight dipole affects the curved element radiation efficiency and thus adds destructively to the total realized gain pattern. This can be solved by changing the distance of separation *d* between the two elements. However, this will disturb the performance of the straight dipole. Another solution will be discussed later on to restore the curved dipole's gain witout impacting the straight dipole's impedance matching and gain levels.

3.3.2 Eight Element Antenna Structure

In this section, the dual antenna integration is extended into an eight element antenna system with dual frequency of operation, directive gain pattern as well as dual polarization. The eight elements are placed along the four edges of the antenna substrate as shown in Figure 21. The antenna susbtrate is placed along the *XY* plane (horizontal plane). For each structure, two elements are oriented along the *x*-axis while the other two are placed along the *y*-axis. Such placement enables the antenna to feature an orthogonal polarization behavior by receiving both polarized waves along the *x* and *y* directions. The dimension of the antenna Rogers 5880 substrate is 11 cm x 7.5 cm. The two straight dipoles (Element 1: S1 and Element 2: S2) are separated by a distance of 83 mm while (Element 3: S3 and Element 4: S4) are separated by a

distance of 51 mm. As for the second structure, the two curved dipoles (C1 and C2) are separated by a distance of 59 mm while (C3 and C4) are separated by a distance of 27 mm. The various distances are greater than the corresponding quarter-wavelength at the dipole's resonant frequency [32].

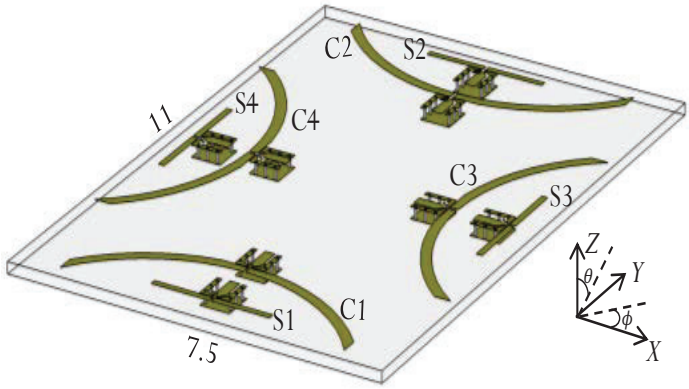

Figure 21. The diversity antenna structure composed of eight radiating elements.

The reflection coefficient of any straight dipole as well as the isolation between S1 and S2, S1 and S3, as well as S3 and S4 are included in Figure 22a. The straight dipole preserves its operation at 4.8 GHz. A good level of isolation is obtained between the various elements due to two factors. First, the distance of separation between the different dipoles is greater than quarter-wavelength and second each straight dipole produces a directional pattern due to the presence of the corresponding curved dipole. The best isolation (-32 dB) is obtained between S1 and S3 since one element is placed along the *x*-direction while the other is along the *y*-direction.

The corresponding S-parameters results for the curved dipoles are shown in Figure 22b. Each curved element resonates at 5.8 GHz. An isolation below -20 dB is obtained between the various elements due to the directional pattern of each curved dipole as well as the corresponding distance of separation. The lowest isolation is obtained between C1 and C3 despite their orthogonal polarization. This behavior is related to the close proximity between these two elements. It is important to note that for either the curved or straight dipoles, the isolation levels between elements 1 and 3, elements 3 and 2, or elements 2 and 4 are identical. In terms of the total gain pattern, each dipole element preserves almost the same characteristics as the dual antenna system. A directive gain pattern towards one of the four quadrants is now achieved. These four quadrants are divided as follows between the various dipole elements for $-180^{o}<\theta<180^{o}$:

Quadrant 1 ($0^{o}<\phi<45^{o}$ and $315^{o}<\phi<360^{o}$) is dedicated for C3 and S3.
Quadrant 2 ($45^{o}<\phi<135^{o}$) is dedicated for C2 and S2.
Quadrant 3: ($135^{o}<\phi<225^{o}$) is dedicated for C4 and S4.
Quadrant 4: ($225^{o}<\phi<315^{o}$) is dedicated for C1 and S1.

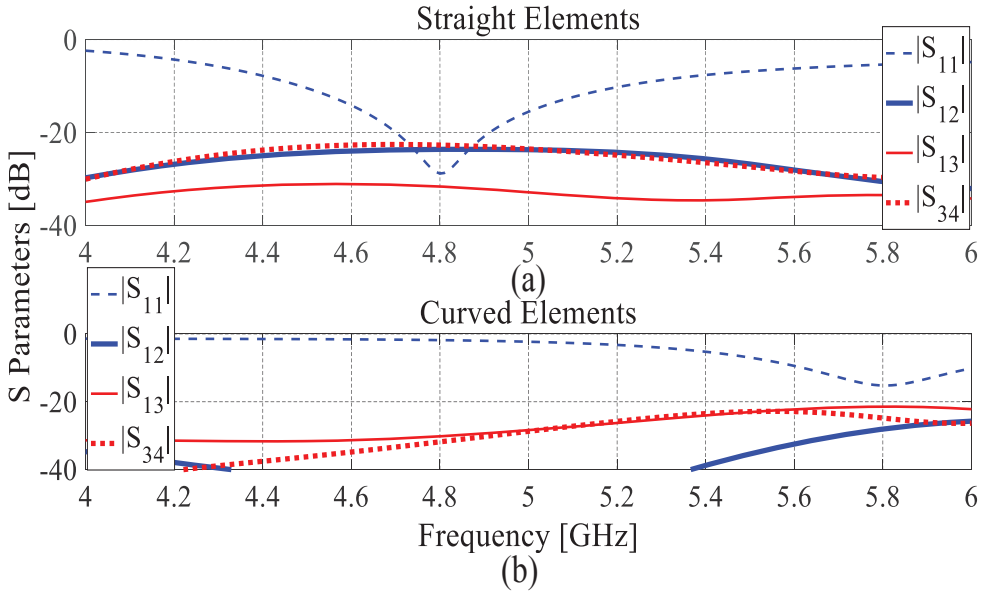

Figure 22. The simulated S-parameters between the various (a) straight dipoles, (b) curved dipoles.

3.3.3 Integration of a Printed Parasitic Reflector

The performance of the antenna system discussed earlier was further enhanced through the integration of a parasitic printed reflector in the center of the top layer as shown in Figure 23. The four edges of the parasitic element have the same curvature and almost the same length as the curved dipoles. Such addition forces each antenna element in the two diversity structures to produce a more directive gain pattern. It also compensates for the drop in the gain levels of the curved dipoles. It is important to note that the addition of this parasitic element doesn't increase the total dimensions of the antenna system since it is placed in the empty space between the four curved elements.

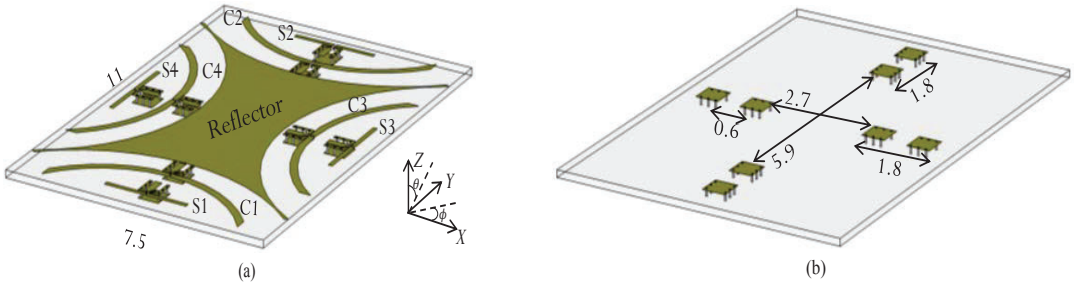

Figure 23. The final antenna structure after the integration of the printed parasitic element (a) Top view, (b) Bottom view.

1) Effect on the input reflection coefficient of any curved and straight dipole:

The effect of the printed reflector on the reflection coefficient of any straight and curved dipole is shown in Figure 24a. The resonant frequency of the curved dipole is shifted from 5.8 GHz to 5.6 GHz. This is due to the inductive effect of the printed parasitic element on the impedance of any curved dipole. The impedance match of the curved dipole is also improved where the reflection coefficient drops from -15 dB at 5.8 GHz to -20 dB at 5.6 GHz. The reflection

coefficient of any straight dipole is also included in Figure 24a. The straight dipole preserves its resonant frequency at 4.8 GHz. This is obtained since the existence of the curved dipole minimizes the effect of the parasitic element on the impedance of the straight dipole.

2) Effect on the isolation between the curved dipoles:

The improvement in the isolation between the curved dipoles C3 and C4 can be inspected in Figure 24b. The isolation level at *f*=5.6 GHz is almost -30 dB after adding the curved parasitic element. On the other hand, the isolation between the curved dipole C1 and C3 remains almost the same. The same behavior applies to the other combination of the curved dipole elements.

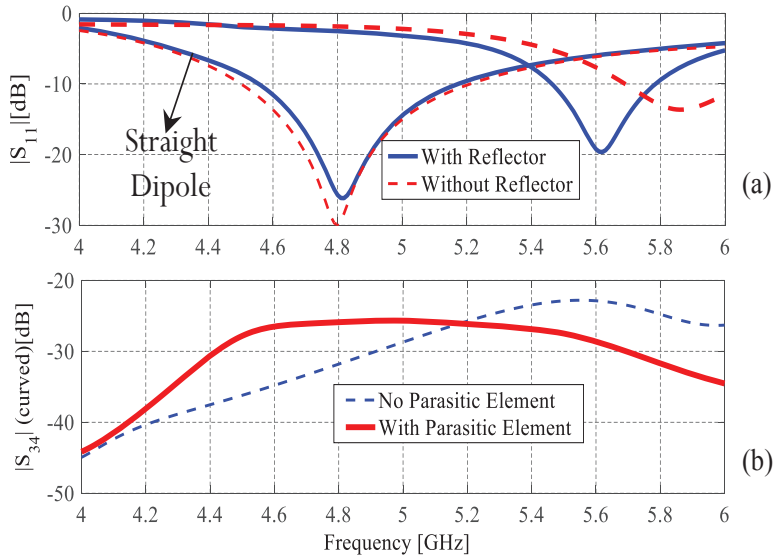

Figure 24. (a) The effect of the printed parasitic reflector on the reflection coefficient of both radiating structures, (b) The change in the isolation between C3 and C4.

3) Effect on the gain pattern of the curved/straight dipoles:

The realized total gain pattern for the two curved dipole elements C3 and C4 after the integration of the printed reflector is plotted in Figure 25a along the *XZ* plane at *f*=5.6 GHz. The gain pattern becomes more directive with a maximum realized gain of 6.7 dBi and a minimal back lobe. The front to back gain ratio has improved from 5.98 dBi without the printed parasitic element to almost 12 dBi. The total gain pattern at *f*=4.8 GHz for S3 and S4 is summarized in Figure 25b along the *XZ* plane. The backlobe gain pattern is reduced from -0.2 dBi (without the parasitic reflector) to almost -10 dBi. As for the peak gain, it retains its maximum value of 4.7 dBi. Figure 25c shows the 3D total gain pattern (top view) when C3 is activated while Figure 25d presents the same data when S2 is fed. These two plots highlight the

directive behavior of the total gain pattern after the integration of the printed parasitic reflector. Each dipole is dedicated to cover a specific quadrant.

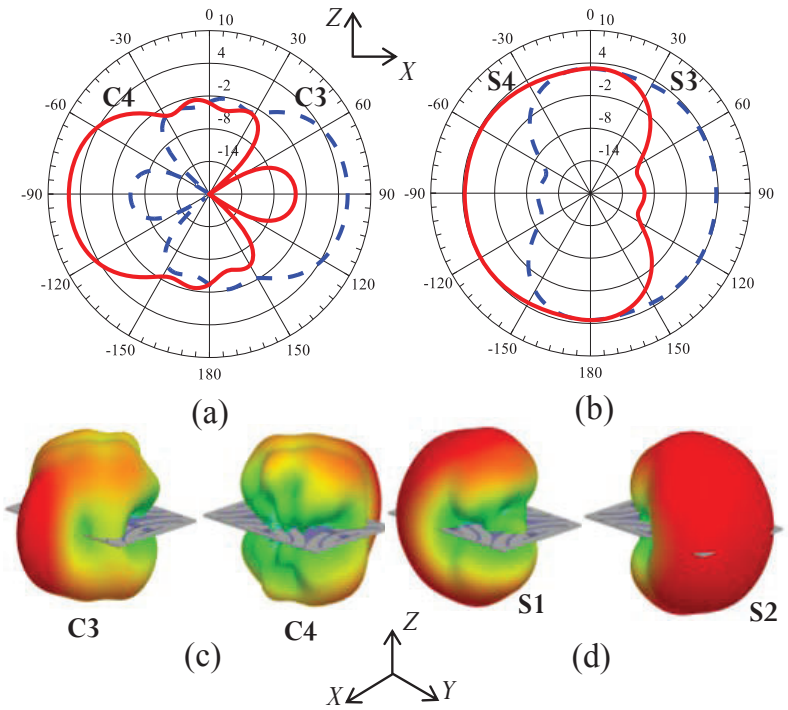

Figure 25. The total gain pattern after the addition of the printed parasitic element for (a) C3 and C4 (*f*=5.6 GHz), (b) S3 and S4 (*f*=4.8 GHz), (c) T3D gain pattern when C3 or C4 is activated (*f*=5.6 GHz) , (d) S1 or S2 is activated (*f*=4.8 GHz).

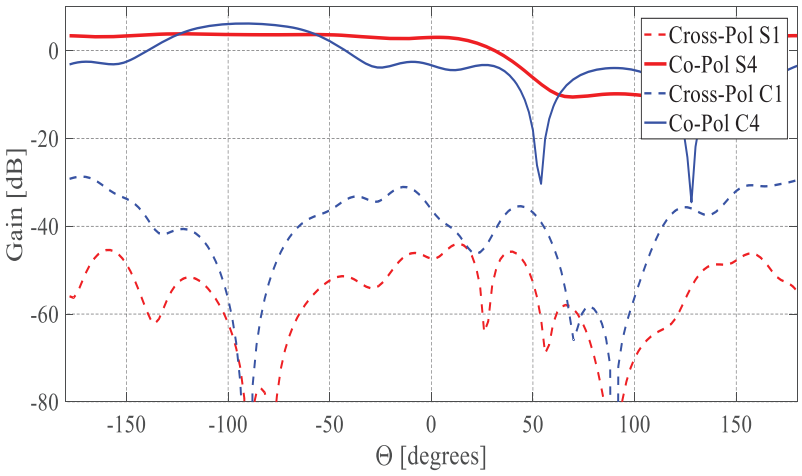

Figure 26. The gain difference between the cross-polarized component of S1/C1 and the co-polarized component of S4/C4.

4) Effect on the polarization of the curved/straight dipoles:

Figure 26 shows the cross-polarized gain component for S1/C1 and the co-polarized gain component for S4/C4. Even though the four polarizations components shown in Figure 26 possess the same sense (*y*-polarized), a noticeable gain difference is obtained between the two straight as well as the two curved elements. Similar results can be obtained between the remaining dipoles. These results confirm that the polarization orthogonality feature is maintained for both structures. Such behavior is mainly related to the placement of the various elements along the four edges of the substrate.

3.3.4 Assessment of the Fabricated Prototype

The proposed antenna system is fabricated to test its performance as shown in Figure 27. Every integrated balun has a ground plane that is optimized to be of the same size as the SMA connector. A hole is drilled throughout the substrate to connect the SMA feeding point to the input lead of the balun. The comparison between the simulated and measured antenna's reflection coefficient when one curved dipole is fed while all the other elements are loaded by 50 Ω terminations is shown in Figure 28. Any curved dipole element covers a measured band from 5.3 GHz-5.85 GHz. The same mechanism is repeated by feeding only one straight dipole and terminating the remaining seven elements by 50 Ω. Any straight dipole element covers the

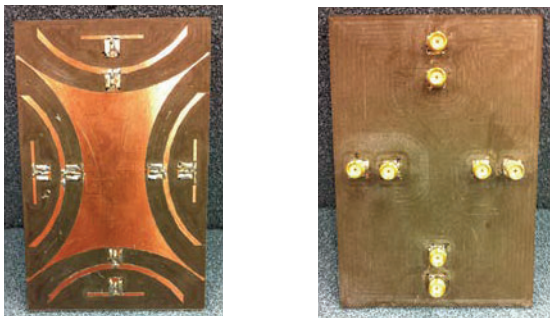

Figure 27. The top and bottom layer of the fabricated prototype.

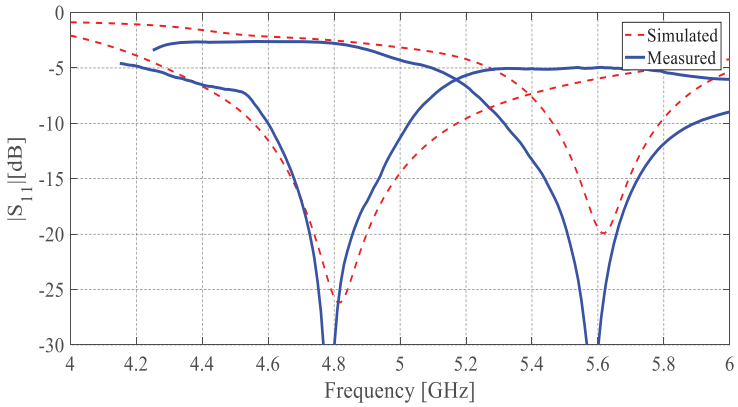

Figure 28. The reflection coefficient of any curved dipole and straight dipole.

band of frequency from 4.6 GHz-5 GHz as also presented in Figure 28. For both measurements, a good agreement is noticed with the computed data.

The simulated and measured total gain pattern in the *XZ* plane are plotted in Figure 29a for the case when S3 or C4 is fed. The patterns for the other straight or curved dipoles are similar but with the main beam directed in other directions according to their respective positions on the antenna system. A measured maximum total gain of 4.5 dBi (S3) and 5.6 dBi (C4) is achieved accordingly. To further investigate the directive behavior of the proposed antenna system, the total measured gain pattern in the *XY* plane is summarized in Figure 29b for the two straight dipoles (S1 and S2) as well as for the two curved dipoles (C3 and C4). Such plot proves that each straight/curved dipole element covers a specific quadrant with a minimal back lobe radiation. The measured isolation between the various straight as well as curved dipoles are summarized in Table 1. The fabricated antenna structure is able to maintain low isolation levels between the different elements. These values agree well with the simulated data presented earlier.

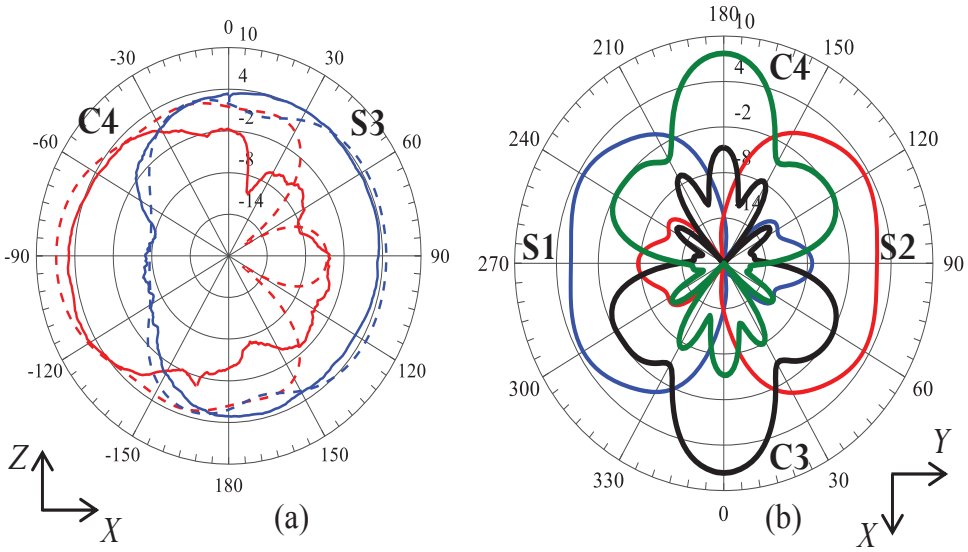

Figure 29. The simulated (dotted line) and measured (solid line) total gain pattern in the *XZ* plane for S3 at *f*=4.8 GHz and C4 at *f*=5.6 GHz, (b) The measured gain for S1, S2, C3, and C4 in the *XY* plane.

Table 1 The measured isolation $|S_{ij}|$ (dB) between the various elements in the two radiating structures

Straight Dipoles (*f*=4.8 GHz)	Curved Dipoles (*f*=5.6 GHz)
$\|S_{12}\|_{dB}$=-41	$\|S_{12}\|_{dB}$ =-31
$\|S_{13}\|_{dB}$ =-30	$\|S_{13}\|_{dB}$ =-28
$\|S_{34}\|_{dB}$ =-28	$\|S_{34}\|_{dB}$ =-28

3.3.5 Diversity System Analysis

The proposed antenna system can be deployed in a multiple-input-multiple output (MIMO) environment with dual operating frequency, directive radiation patterns and dual polarization. The antenna system can be considered as a two 4-elements MIMO structure. The first structure is composed of the straight elements while the second one consists of the curved elements. It is important to note that the entire antenna strucutre is placed along the *XY* plane (horizontal plane) as detailed in Figure 23. To assess the performance of the proposed antenna system, its corresponding envelope correlation coefficient (ECC), mean effective gain (MEG) of each branch, the MEG ratio between the diversity branches, the diversity gain (DG), and the total active reflection coefficient (TARC) are characterized [33]. For both dipoles diversity structures, there are four branches where each branch corresponds to one of the radiating elements.

The performance of the two structures are studied under different scenarios by taking into account the statistical propagation properties of both vertically and horizontally polarized incoming multipath signals. Three different statistical distributions (Gaussian, Laplacian, and elliptical) for the incoming signals are considered in this work. For the Gaussian and Laplacian cases, the power spectrum of the incoming signals in the azimuth plane is considered to be uniform. As for the elliptical case, the power of the incoming signals is shaped in both the elevation and azimuth planes [34-37]. Table 2 summarizes the ECC, MEG of each branch, and MEG ratio between C1 and C2, C3 and C4, as well as C2 and C3 for the curved dipole diversity structure at f=5.6 GHz. The same data sets are also presented in Table 2 between the different elements of the straight dipole structure (S1 and S2, S3 and S4, S2 and S3) at f=4.8 GHz.

For the three different channel models in both an indoor and outdoor environment, the two structures are able to exhibit an excellent performance. An ECC close to zero is attained thus ensuring the independence between the different incoming fading signals in a multipath environment. The MEG of any straight or curved dipole element shown in Table 2 takes into account the radiation power pattern and the efficiency of the corresponding element as well as the statistical propagation properties of both vertically and horizontally polarized multipath incident radio waves. The MEG ratio between the corresponding dipole elements in both structures is very close to unity. This indicates that the power received by each antenna branch is almost the same. For each dipole combination shown in Table 2, MEG1 corresponds to either element C1, C2, C3, S1, S2, or S3, while MEG2 corresponds to C2, C3, C4, S2, S3, or S4.

An almost similar maximum ratio combining diversity gain (DG_{MRC}) is obtained for the different scenarios shown in Table 2 between the curved dipoles at f=5.6 GHz and the straight dipoles at f=4.8 GHz. A diversity gain between 11.4 and 11.7 dB is achieved for the different cases. The diversity gain is calculated for a 1% probability level and by assuming a Rayleigh fading channel with the noise being equal and uncorrelated between the antenna branches. The

diversity gain is also computed by replacing the average signal to noise ratio with the corresponding MEG.

Table 2. Envelope correlation coefficient (ECC), mean effective gain (MEG), and diversity gain for various hypothetical scenarios

Propagation Model	Environment	Radiating Elements	ECC	MEG1 [dB]	MEG2 [dB]	MEG Ratio	DG_{MRC}[dB]
Gaussian	Outdoor	C1-C2/**S1-S2**	1.1×10^{-3}/**6.7×10^{-3}**	-5.34/**-6.9**	-5.35/**-6.9**	0.97/**0.99**	11.7/**11.6**
		C3-C4/**S3-S4**	2.4×10^{-3}/**2.1×10^{-1}**	-5.89/**-6.38**	-6.02/**-6.35**	0.97/**0.99**	11.6/**11.6**
		C2-C3/**S2-S3**	4.2×10^{-3}/**6.1×10^{-3}**	-5.51/**-6.99**	-5.81/**-6.45**	0.93/**0.88**	11.6/**11.6**
	Indoor	C1-C2/**S1-S2**	1.5×10^{-4}/**8.3×10^{-4}**	-3.05/**-4.04**	-2.94/**-4.04**	0.97/**0.99**	11.6/**11.6**
		C3-C4/**S3-S4**	3.1×10^{-1}/**6.2×10^{-5}**	-3.53/**-3.81**	-3.58/**-3.81**	0.98/**0.99**	11.6/**11.6**
		C2-C3/**S2-S3**	5.9×10^{-3}/**5.8×10^{-4}**	-3.05/**-4.03**	-3.54/**-3.86**	0.89/**0.96**	11.7/**11.6**
Laplacian	Outdoor	C1-C2/**S1-S2**	7.5×10^{-4}/**7.8×10^{-3}**	-5.36/**-6.79**	-5.24/**-6.79**	0.97/**0.99**	11.5/**11.6**
		C3-C4/**S3-S4**	9.8×10^{-4}/**6.9×10^{-6}**	-5.64/**-6.14**	-5.75/**-6.11**	0.97/**0.99**	11.6/**11.6**
		C2-C3/**S2-S3**	2.7×10^{-3}/**6.1×10^{-2}**	-5.37/**-6.78**	-5.56/**-6.22**	0.96/**0.87**	11.5/**11.6**
	Indoor	C1-C2/**S1-S2**	2.3×10^{-4}/**9.9×10^{-4}**	-3.35/**-4.18**	-3.25/**-4.18**	0.97/**0.99**	11.4/**11.7**
		C3-C4/**S3-S4**	7.1×10^{-4}/**6.9×10^{-6}**	-3.81/**-3.93**	-3.88/**-3.92**	0.98/**0.99**	11.7/**11.6**
		C2-C3/**S2-S3**	8.4×10^{-3}/**8.4×10^{-4}**	-3.36/**-4.16**	-3.81/**-3.98**	0.90/**0.84**	11.8/**11.7**
Elliptical	Low Directivity (Indoor/Outdoor)	C1-C2/**S1-S2**	7.3×10^{-3}/**9.7×10^{-3}**	-4.20/**-1.77**	-4.40/**-1.75**	0.95/**0.99**	11.6/**11.6**
		C3-C4/**S3-S4**	1.1×10^{-3}/**4.8×10^{-4}**	-3.93/**-4.15**	-3.91/**-4.15**	0.99/**0.99**	11.6/**11.6**
		C2-C3/**S2-S3**	3.9×10^{-3}/**1.4×10^{-3}**	-4.20/**-3.79**	-3.96/**-4.07**	0.94/**0.93**	11.7/**11.6**
	High Directivity (Indoor/Outdoor)	C1-C2/**S1-S2**	2.9×10^{-3}/**3.1×10^{-3}**	-4.81/**-3.30**	-5.16/**-2.33**	0.92/**0.81**	11.6/**11.6**
		C3-C4/**S3-S4**	5.9×10^{-5}/**5.6×10^{-3}**	-3.38/**-2.74**	-3.34/**-2.74**	0.98/**0.99**	11.6/**11.6**
		C2-C3/**S2-S3**	6.4×10^{-3}/**1.4×10^{-3}**	-3.79/**-2.37**	-3.34/**-2.62**	0.91/**0.94**	11.7/**11.7**

The diversity gain of the proposed structure is also assessed for both random-LOS and rich isotropic multipath (RIMP) propagation scenarios [38-40]. These two scenarios are studied as well since real-life environments are somewhere in between random-LOS and RIMP. If an antenna structure is tested with good performance in these two environments, then it will also perform well in real-life environments, including the space environment [41]. The diversity gain between the various dipole elements for both models is summarized in Table 3. Figure 30a shows the diversity gain between the four curved dipoles in random-LOS environment while Figure 30b presents the case for the four straight dipoles for the RIMP scenario. A

diversity gain of almost 16.5/18.9 dB is achieved for the four curved dipoles (random-LOS/RIMP) while the four straight dipoles feature a diversity gain of 16.7/19.1 dB (random-LOS/RIMP). Such level of diversity gain is obtained due to the high isolation between the dipole elements as well as the directive gain pattern of the curved and straight dipoles. These results prove the validity of the proposed antenna structure as a diversity structure in a high multipath environment.

Table 3 The diversity gain [dB] for both Random-LOS and RIMP scenarios

Radiating Elements	Random-LOS	RIMP
C1-C2/**S1-S2**	10.2/**7.2**	11.5/**11.7**
C3-C4/**S3-S4**	7.6/**10.6**	11.8/**11.7**
C2-C3/**S2-S3**	8.9/**7.4**	11.7/**11.6**

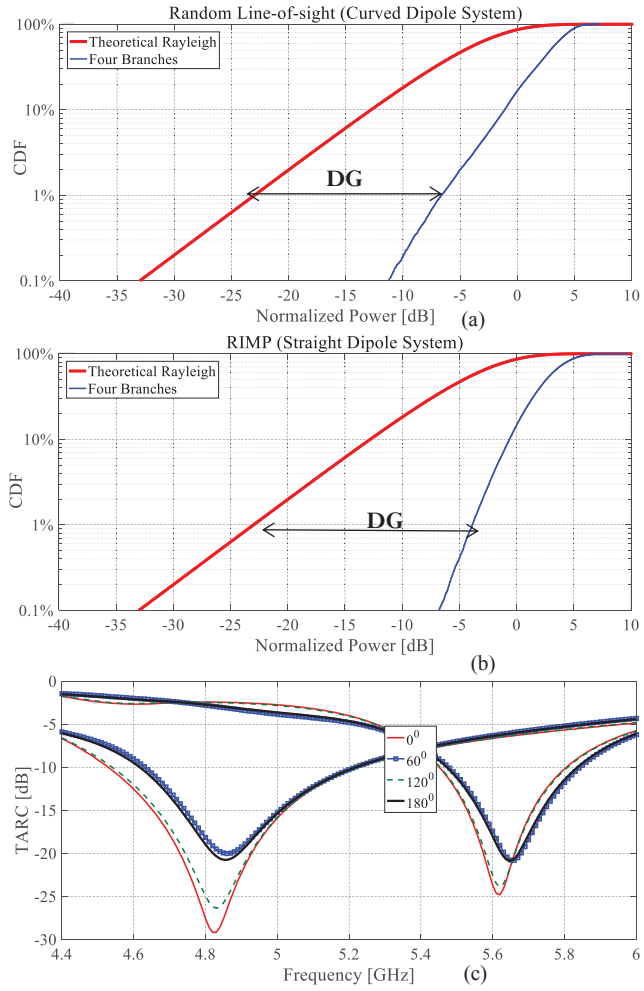

Figure 30. The cumulative distribution function for the (a) four curved dipoles (random-LOS), (b) four straight dipoles (RIMP), (c) The TARC between S1 and S2 as well as C1 and C2 for various phase differences.

Another parameter to take into consideration in such analysis is the TARC. The objective of such study is to guarantee that the power delivered to each dipole element is radiated. The TARC determines the resonant frequency and the impedance bandwidth of the MIMO structure as a function of the phase excitation between the various dipole elements. The TARC (dB) between S1 and S2 as well as between C1 and C2 are shown in Figure 30c for four different values of the phase difference. Based on this plot, it is apparent that the proposed structure preserves its operating bandwidth despite the difference in phase between the received signals by the different elements. A similar response is obtained when inspecting the other curved or straight elements in both structures.

The total radiation efficiency of C3 and S3 in both structures is found to be 0.81 and 0.87. The efficiency is computed at the resonant frequency of the corresponding element and by accounting for the coupling between C3 or S3 and all the remaining elements in both structures. Such efficiency is very similar to a standalone curved and dipole element. This proves that the diversity implementation doesn't deteriorate the radiation efficiency of each element due to the high isolation levels between the various dipoles.

3.3.6 Control of the System's Radiating Elements

The operation of each diversity structure is controlled by integrating a reconfigurable feeding network. The purpose of the network is to selectively enable each structure to radiate on demand as illustrated in Figure 31a. The structure of the proposed reconfigurable feeding network is shown in Figure 31b. It is printed on a Rogers 3203 substrate with a dielectric constant of 3.02 and a thickness of 1.52 mm. It has an overall dimension of 3.5 cm x 3.5 cm and consists of three ports. Port 1 is the input port where the RF signal is supplied. The two output ports (Port 2 and 3) are used to feed one straight and one curved dipole. Two PIN diodes (D_1 and D_2) are appropriately incorporated in the network's structure as shown in Figure 31b. These PIN diodes allow the RF input signal to be delivered to either Port 2 or Port 3.

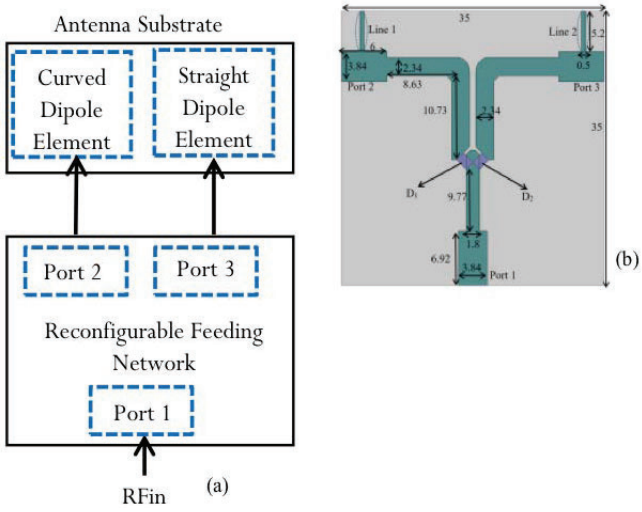

Figure 31. (a) The control of two different radiating elements via a reconfigurable feeding network, (b) The physical dimensions of the proposed reconfigurable feeding network

The reconfigurable feeding network is composed of multiple microstrip transmission lines with appropriate impedances to satisfy matching criteria. The first transmission line, where the input signal is supplied, has a width of 3.84 mm. This width corresponds to an input impedance of 50 Ω. The second transmission line has a length of 9.77 mm and a width of 1.8 mm. This length value is designed to match the 50 Ω input to the input impedance of the two PIN diodes (D_1 and D_2). The length of the second transmission corresponds to $\lambda_g/4$ at 5 GHz. The output of each PIN diode is connected to a 90^0 curved transmission line with a total length of 19.36 mm ($\lambda_g/2$ at 5 GHz) and a width of 2.34 mm. The last transmission line that is connected to port 2 and 3 has an impedance of 50 Ω. The activation of the two PIN diodes is done separately through an external bias tee that guides the RF signal and supplies the necessary DC current level. The PIN diodes used in this paper are BAR 64 from Infineon technologies [42].

Two biasing lines (lines 1 and 2), as highlighted in Figure 31b, are used to provide a closed path to the DC current that flows through each PIN diode from the external bias tee. Once connected to the ground of the feeding network, the corresponding PIN diode is activated.

Figure 32a compares the simulation and measurement of the reflection coefficient at the input port (Port 1), the reflection coefficient at the output port (Port 2), and the transmission from port 1 to port 2 when both diodes are OFF. There is no matching at the two ports. The corresponding reflection coefficients are higher than -10 dB. Besides reflection losses, a weak transmission is witnessed. This is due to the fact that during the OFF-mode, the diodes block the RF signal from being delivered to the corresponding output port. Figure 32b shows the same data but for the case when diode D_1 is activated. The reflection coefficient at port 1 and port 2 is below -10 dB over the 4-6 GHz frequency span. The measured insertion loss is not more than -2 dB for the whole frequency range of interest.

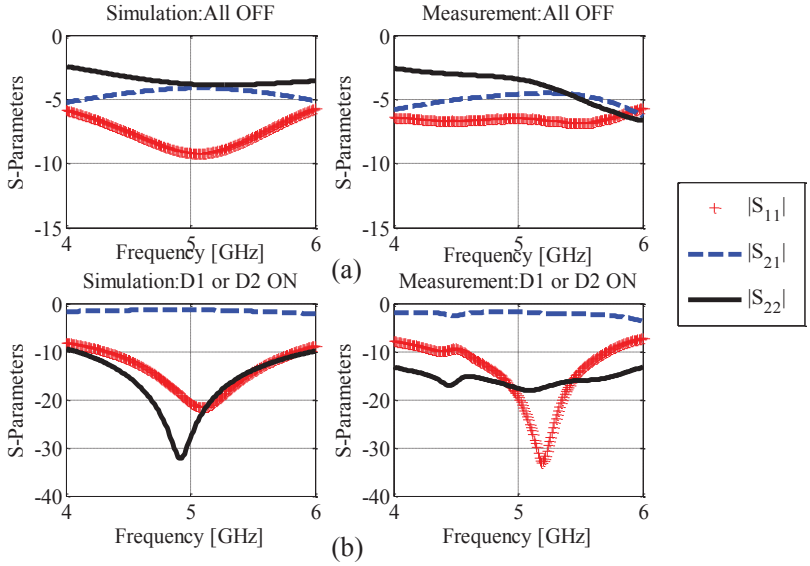

Figure 32. The comparison between the simulated and measured S-parameters of the feeding network (a) when both diodes are OFF, (b) when D1 or D2 is ON

Four networks are required to feed the different dipoles of both structures. The integration of the four networks with the antenna structure is demonstrated in Figure 33a. Each network is placed at the bottom layer of the antenna and orthogonal to the printed parasitic curved reflector. The ground plane of each feeding network is facing the corresponding set of dipole elements. Such placement guarantees that the radiation from the different antenna elements does not affect the operation of the four networks. Each feeding network contains two PIN diodes and in total four diodes must be activated simultaneously in order to feed either the four straight or curved elements. Diodes D1, D3, D5 and D7 that are shown in Figure 33b must be activated simultaneously to feed all the four curved elements. The feeding of the four straight elements is done by biasing the other four diodes (D2, D4, D6 and D8). The corresponding fabricated prototype is shown in Figure 33c.

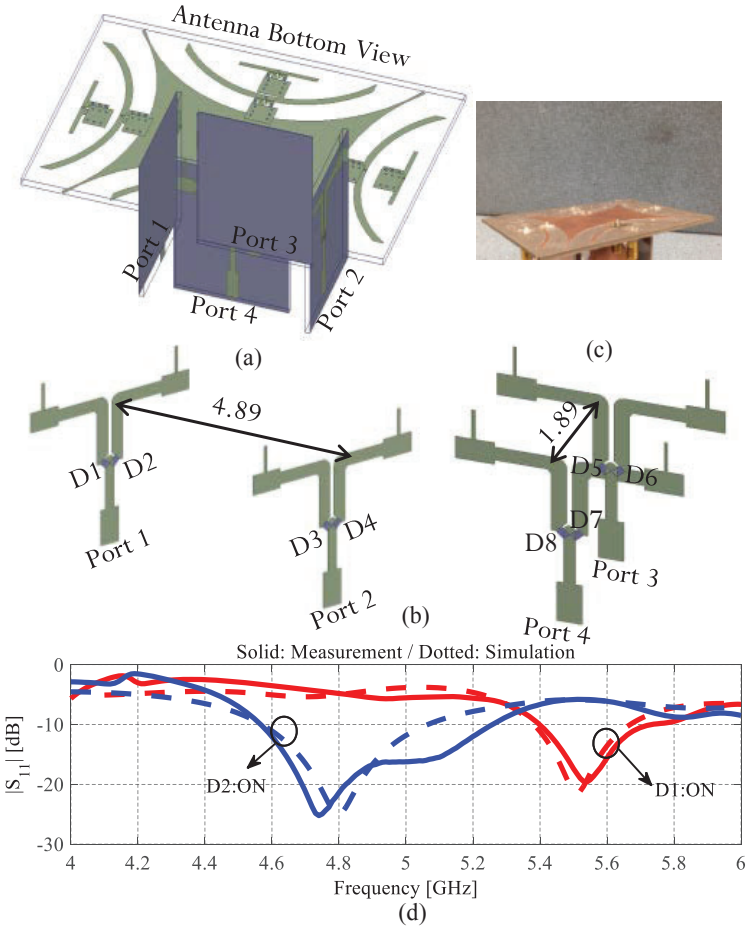

Figure 33. (a)The bottom view of the integration of the four feeding networks underneath the curved printed reflector, (b) The location of the eight diodes within the four feeding networks, (c) The fabricated prototype, (d) The simulated and measured reflection coefficient.

The comparison between the simulated and the measured reflection coefficient at the input port 1 of the feeding network is plotted in Figure 33d. The simulated results are obtained by modeling the antenna system as an 8 port S-parameters matrix while each feeding network is modeled as a 3 port S-parameters matrix. The connections between the two output ports of the feeding network and the antenna elements are achieved through low loss flexible coaxial cables. The lengths and losses of these cables are included in the simulation to account for their effect on the antenna matching performance. The same response can be obtained when activating the other diodes in the three different feeding networks.

The total gain patterns for the various elements are affected by the integration of the four feeding networks within the antenna system. The transmission between the input port of each feeding network and one of its two output ports as well as the insertion loss of any biased PIN diode have an effect on the gain level of the corresponding radiating element. The measured gain pattern along the *XZ* plane when the curved element C3 is fed directly without the presence of the feeding network is shown in Figure 34a. The same data is plotted when C3 is fed through the third feeding network and by activating the diode D5. Two different scenarios for the feeding networks are investigated. The first scenario corresponds to the case when the

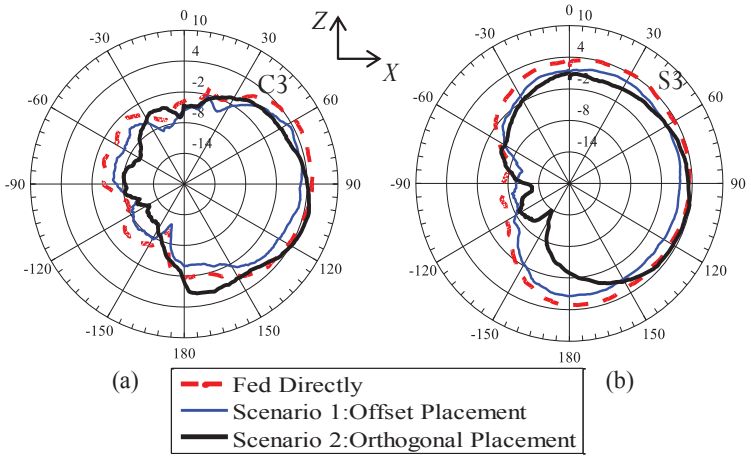

Figure 34. The change in the measured gain pattern with and without the reconfigurable feeding network when feeding (a) C3, (b) S3

Table 4 The measured isolation $|S_{ij}|$ (dB) between the input ports of the four feeding networks

Straight Dipoles (f=4.8 GHz) D2, D4, D6, D8: ON	Curved Dipoles (f=5.6 GHz) D1, D3, D5, D7: ON
$\|S_{12}\|_{dB}$=-36.4	$\|S_{12}\|_{dB}$ =-38.2
$\|S_{13}\|_{dB}$=-38.7	$\|S_{13}\|_{dB}$ =-39.9
$\|S_{34}\|_{dB}$=-32.5	$S_{34}\|_{dB}$ =-35.2

feeding networks are not placed orthogonally to the printed curved reflector. The four feeding networks are located at an offset position away from the antenna structure. The purpose of this scenario is to assess the effect of the insertion loss of the reconfigurable feeding network on the antenna gain pattern. For this scenario, the measured total gain drops from 5.6 dBi to 4.2 dBi. The second scenario, also shown in Figure 34a, assesses how the ground plane of each feeding network helps in compensating the drop in the gain levels. By placing the four reconfigurable feeding networks orthogonal to the printed parasitic reflector, the maximum achieved total gain for the curved elements increases to 5.3 dBi. The back lobe of the gain pattern also decreases. The measured isolation |Sij| (dB) between the input ports of the four feeding networks are shown in table 4.

The same behavior is obtained for the remaining curved dipoles. Figure 34b shows the same set of data but for the case when the straight element S3 is fed. The maximum measured total gain drops from 4.5 dBi to 2.7 dBi after feeding the radiating element through the corresponding feeding network. The orthogonal placement of the four networks allows each straight dipole to achieve a maximum measured gain of 4.3 dBi with a decrease in the backlobe gain pattern. The direction of the maximum realized gain for both the curved and straight elements shifts from θ=90^{o} to almost θ=110^{o} as highlighted in Figure 34. This shift is related to the placement of the feeding network orthogonally underneath the bottom layer of the antenna substrate.

As a summary, it is important to highlight the key differences between the work presented here and recently published work on diversity antenna structures [23-29]. First, the system proposed in this paper features two compact antenna diversity structures that operate at two distinct spans of frequencies. Each antenna structure actively contributes in shaping the gain pattern of the other structure, thus improving the directional behavior of each antenna element and increasing the isolation levels between the different elements. The proposed work is to our knowledge the first reported antenna system that features feeding reconfigurability between the two diversity structures. The reconfigurable feeding network is designed to choose which diversity structure to activate while at the same time compensating for all the losses that result from the activation of the integrated PIN diodes. Also, in this work, the diversity gains from each four curved or straight elements varies between 16.5 dB and 19.1 dB. As for [43], the authors are able to achieve a gain of 13.6 dB when relying on four folded dipole elements. The gain increases to 17.0 dB when adopting eight dual polarized elements. Another diversity antenna array that consists of eight antenna elements is discussed in [44]. The structure has four horizontally oriented and the remaining four are vertically oriented with a reported diversity gain of 9.5 dB.

3.4 Integrating Antenna Arrays over Solar Cells for Dual Source of Energy Harvesting

In this section we discuss the design of two antenna arrays that operate from 1.8 GHz till 2.4 GHz. The antenna arrays are composed of two elements each and are proposed for RF energy harvesting. The idea is to develop antenna that can be used on cubesats for both communication and RF harvesting purposes. The antenna arrays are integrated vertically on top of a solar panel, from opposite edges. Copper based inverted-F antennas constitute the elements of both antenna arrays. Two transparent antenna arrays of same physical dimensions and topologies as the copper ones are also investigated. The transparent arrays' investigation aims to validate the integration of the copper based inverted-F antenna arrays on top of the solar panel. A rectifying circuit that is positioned at the output of both arrays is also designed and tested. The measured performance results of the fabricated prototypes for the two arrays as well as the rectifying circuit show good agreement with the simulated data.

The harvesting and rectification of ambient electromagnetic waves into DC voltage is an important and needed feature for any battery dependent device and a cubesat structure. The main objective in any energy harvesting system is increasing its efficiency. The efficiency of the harvesting antenna is at the core of this design constraint and must be taken with extreme care and consideration. A suitable antenna structure must exhibit enough gain levels to capture as much as possible from the ambient RF signals that span over a wide range of frequencies. Another constraint that must be satisfied is related to the efficiency of RF rectification into DC signals. A design of the appropriate rectifying circuit must be matched to the antenna structure as well as the incorporation of the corresponding power management circuitry [45]. The combination of an antenna and a rectifying circuit is called a "rectenna".

Harvesting efficiency is increased when antennas are integrated on top of solar panels. The antennas must have a minimal effect on the solar panels to allow for a full solar energy harvesting capability during the daytime. The antennas become the sole source of energy harvesting during night time and that could be very advantageous in powering future cubesats. Thus, a continuous dual source energy harvesting can be achieved by such integration. Planar antenna structures on top of amorphous silicon (a-Si) solar cells for dual source of energy harvesting were used in [46] with a good rectification efficiency.

Transparent radiating structures can be seen as alternative radiating elements on top of solar panels for the harvesting of electromagnetic waves. Such elements are designed by relying on transparent conductive oxides such as ITO or AgHT. As an example, the authors in [47] designed an AgHT based transparent ultra-wideband antenna. The antenna is sandwiched between a glass superstrate and a solar panel.

In this work, the design of a copper based antenna array structure to be integrated on top of a solar cell was studied. The work discussed here is a continuation of the work presented in [48, 49]. Two arrays were first designed based on copper based inverted-F antenna elements. The positioning of the antenna elements was optimized to minimize sunlight blockage. The antenna arrays structure insure that the solar cell's harvesting efficiency does not degrade despite the fact that the antenna elements are copper based. This verified by building similar transparent antenna arrays and comparing the system's output voltage. On the other hand, the integrated solar panel enhances the radiation characteristics of the proposed designs by acting as an extended ground plane. The antenna elements are designed to cover a wide bandwidth from 1.8-2.4 GHz, thus covering most of the commercial RF signals that can be available for harvesting. An RF rectifying circuit was also designed to be able to rectify the captured RF energy into useful DC power that can be combined with the output of the solar panels.

This work differs from previously reported designs by various factors. Its novelty is based on the fact that the dual source harvesting is achieved without relying on transparent conductive materials that are mainly expensive and require extensive care when used as radiating elements at RF frequencies. In addition, the array vertical topology allows for easier solar panel integration without affecting the solar panel's sunlight exposure. Thus, the full system relies from the advantages of copper based antennas in terms of gain and efficiency in addition to the full energy harvesting of a solar panel. The rectified RF energy and the solar panel voltage output are proposed to constitute a dual source of needed energy.

3.4.1 Single Element Design

The antenna structure that was investigated here is a copper-based inverted-F antenna of thickness 0.5 mm. Such structure enables good integration with a solar panel since it has a low profile and thus ensures that the sunlight will not be blocked during day time. The operating bandwidth of interest is from 1.8 GHz till 2.4 GHz. Our experimental results have proven that this band of frequencies is one of the busiest bands available around our geographical location and thus constitute a suitable candidate for RF harvesting purposes, but the design can be adapted to any range of frequencies.

Figure 35 shows the proposed inverted-F antenna placed orthogonal to the upper edge of the a-Si solar panel. The panel has a length of 15 cm, a width of 8 cm and a thickness of 220 μm. The bottom layer of the panel is coated by an aluminum layer. This layer is extended by an additional aluminum sheet of the same length of 15 cm but with a width of 5 cm. A shorting arm of length 1.547 cm, width 0.2 cm and at an offset distance of 0.475 cm from the feeding line is added to compensate for the capacitive effect between the antenna arm and the ground plane. The width of the extended layer affects the gain pattern characteristics of the inverted-F antenna. Figure 36a shows the antenna reflection in function of various widths of the extension.

The reflection coefficient is plotted in function of widths that vary from 1 cm to 9 cm. It is shown that the antenna preserves its matching condition. This can be interpreted by the fact that the antenna's input impedance is mainly affected by the shorting pin and the solar cell is already acting as ground plane for the antenna structure. As the ground plane increases in size, the matching of the antenna improves. This is expected since the operation of the inverted-F antenna is highly dependent on the dimensions of its ground plane.

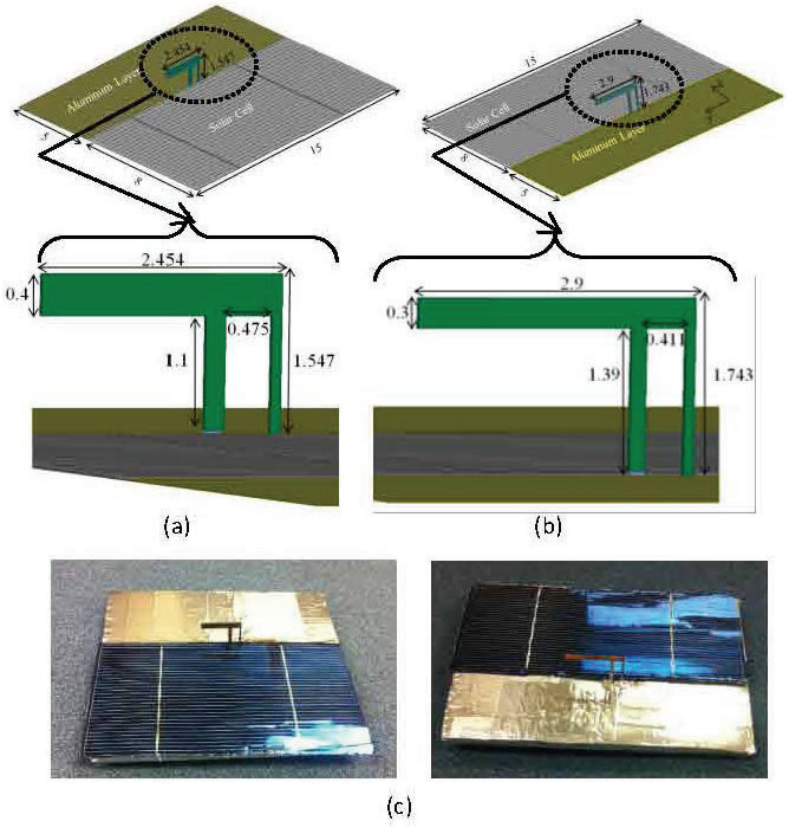

Figure 35. The detailed dimensions of the antenna structure operating at (a) the upper band, (b) the lower band, (c) the fabricated prototypes for both structures.

The effect of the ground plane is clearer in the gain patterns that are shown in Figure 36b for both Φ= 0° and 90° planes at f=2.29 GHz. As the ground plane width increases, the antenna becomes more gainful until it exhibits a maximum gain of 4.6 dB for a width of 5 cm. Beyond a width of 5 cm, the gain ceases to increase any further, however the back lobe is noticeably reduced. Based on this analysis, the extended ground plane for the antenna structure shown in Figure 35a is designed with a width of 5 cm.

The comparison between the simulated and measured reflection coefficient for the inverted-F antenna placed at the upper edge of the solar panel is summarized in Figure 36. The fabricated prototype covers the bandwidth from almost 2.1 GHz up till 2.4 GHz. Since the lowest operating frequency must be 1.8 GHz, a second inverted-F antenna is placed on the opposite

side of the first one and orthogonal to the lower edge of the solar panel. The dimensions of the second inverted-F antenna are summarized in Figure 35b. Similar to the first case, the solar panel acts also as a ground plane for the second structure and an extended ground plane of width 5 cm is added to insure acceptable radiation characteristics for the new antenna elements. In order to cover the lower band, the new added antenna elements have larger dimensions. A shorting arm of length 1.743 cm and with an offset distance of 0.411 cm is introduced in order to achieve an acceptable matching at the antenna input port.

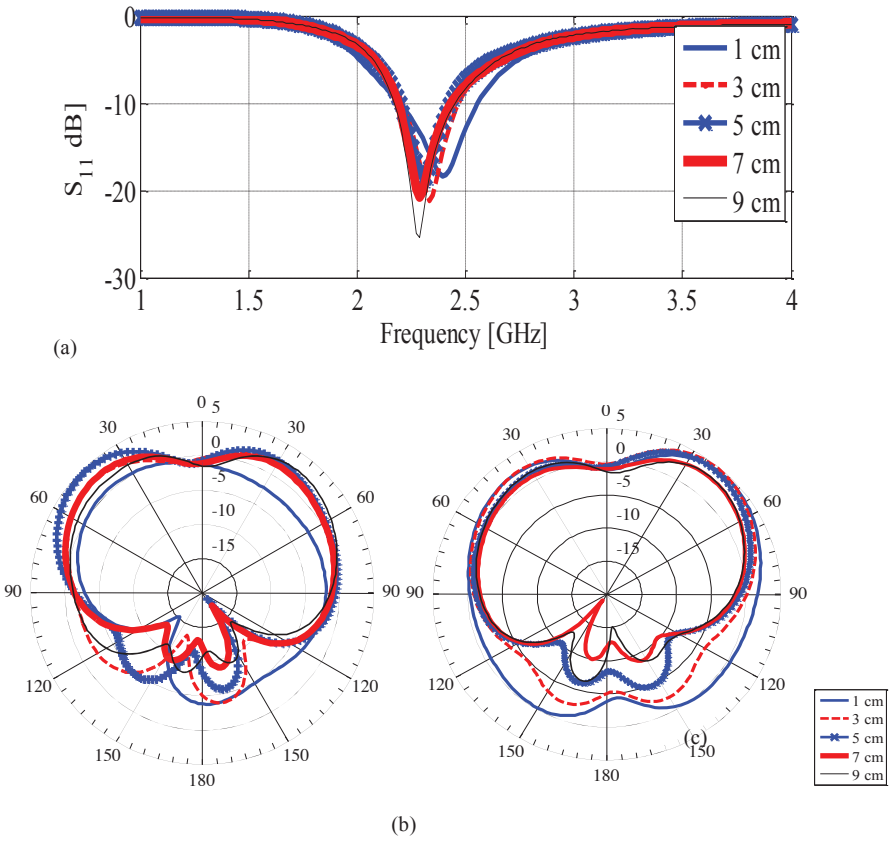

Figure 36. The effect of the width of the extended ground plane on the antenna's (a) reflection coefficient, (b) gain pattern in the Φ= 0° plane, (c) and 90° plane.

The comparison between the simulated and measured reflection coefficient are also included in Figure 37. The new antenna elements cover the bandwidth from almost 1.8 GHz up till 2 GHz. Thus, the incorporation of both structures together, one at the upper edge of the solar panel while the second one at the lower edge, covers the required 600 MHz of operational bandwidth. The fabricated prototypes along with the integrated solar panels for both structures are shown in Figure 35c.

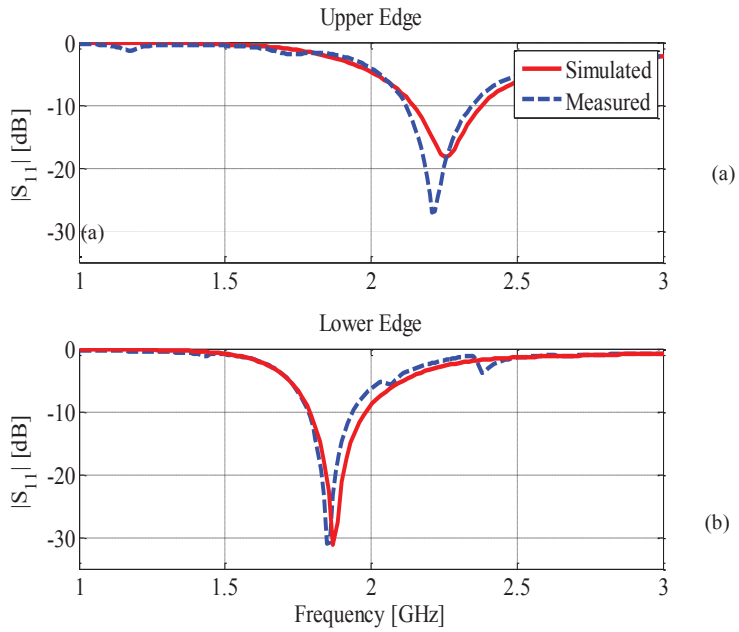

Figure 37. The simulated and measured reflection coefficient for the inverted-F antenna placed (a) at the upper edge, (b) lower edge of the solar panel

3.4.2 Array Implementation

Increasing the antenna effective aperture enhances the antenna gain which improves its ability to harvest RF energy signals. Such task is achieved by resorting to array structures. To that extent, two antenna arrays were designed to cover the required operating bandwidth. The first array covers the upper band and it is located on one edge of the solar panel while a second array is integrated on the opposite edge to cover the remaining frequency bands. The proposed array structures are shown in Figure 38. Each array is composed of two inverted-F antenna elements. Elements 1 and 2 share the same dimensions as the element shown in Figure 35a and thus they cover the upper band. The lower band is covered by elements 3 and 4. These elements share the same dimensions as the inverted-F antenna highlighted in Figure 35.

The two arrays along with their solar panel and extended ground planes occupy an area of 18 cm x 15 cm. The solar panel is incorporated between the antenna elements and it acts as a ground plane for the two arrays. The extended ground plane is composed of an aluminum layer of width 5 cm. The ground plane is extended from both sides of the antenna arrays. The distance of separation between the first two elements is 5 cm while for the other two elements is set to be 4.7 cm. These two distances of separation guarantee that the antenna elements are well isolated and add constructively to the total gain pattern without introduction of nulls in the main lobe.

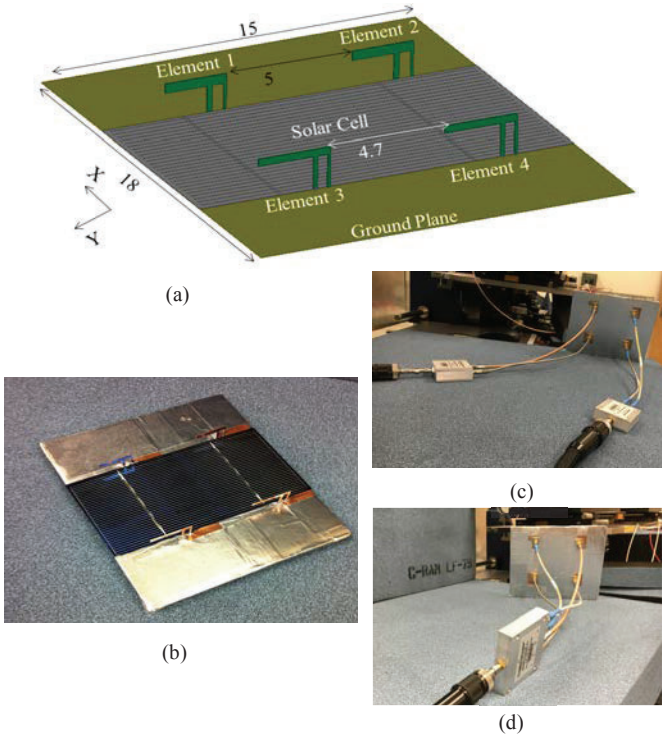

Figure 38. The physical array structure over a solar cell, (b) The fabricated array structure with the solar panel, (c) The feeding of the two array for scenario 3, (d) and scenario 4.

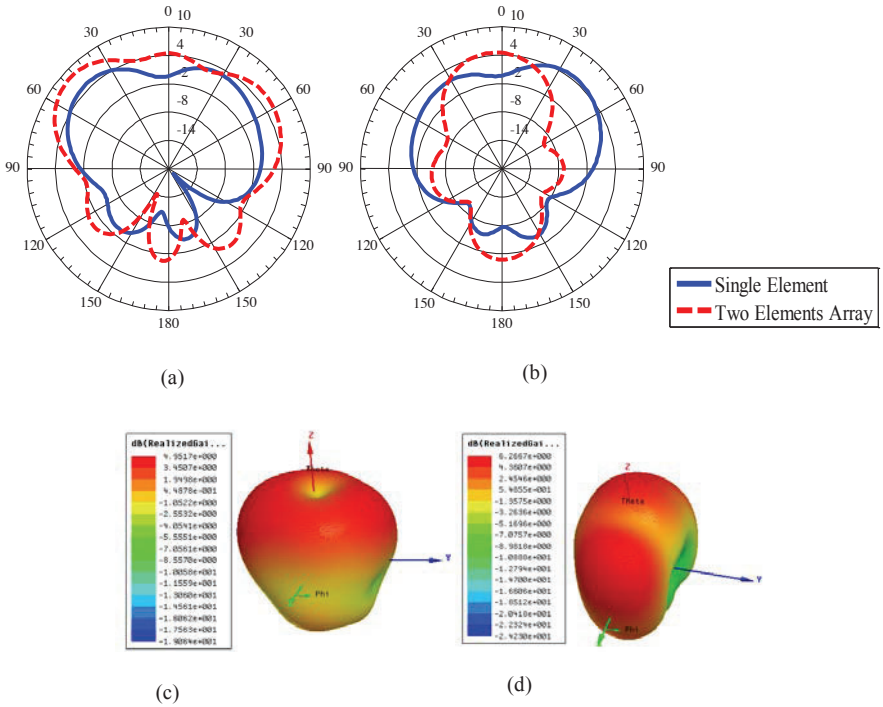

Figure 39. The change in the gain pattern at *f*=2.29 GHz for (a) *Φ*= 0º, (b) *Φ*= 90º, (c) The 3D gain pattern at *f*=1.87 GHz for the one element antenna, (d) The change in the 3D gain pattern for the two elements array (Elements 3 and 4).

Figure 39 shows the effect of implementing an array structure on the total realized gain patterns. The comparison of the 2D gain pattern between one element antenna structure and two elements array at f=2.29 GHz is highlighted in Figures 39a and 39b for both Φ= 0° and Φ= 90° cut planes. The realization of the array structure forces the gain pattern to be more directive and thus an increase in the maximum gain with a value of 8.5 dB is achieved. A similar behavior is obtained for the second array structure that is located at the lower edge of the solar panel. Such an effect can be further highlighted by comparing the 3D gain patterns at f= 1.87 GHz in Figures 30c and 39d. The maximum realized gain increases from 4.9 dB to 6.3 dB. The second array features lower maximum gain than the array located at the upper edge of the solar panel. This is related to the fact that both arrays have an extended ground plane of same width (5 cm). The extended width is kept the same from both sides of the solar panel in order not to disturb the symmetry of the structure.

The initial testing of the proposed structure is executed by feeding one element and terminating the three remaining elements with a matched load. The comparison between the simulated and measured reflection for elements 1 and 4 are plotted in Figure 40a. The same results are obtained if the other elements are fed respectively. As expected, elements 1 and 2 cover almost the band 2.1 GHz up till 2.4 GHz while the other two elements cover the lower band from 1.8 GHz up till 2 GHz. The measured isolation between the various elements is included in Fig. 40b. A minimum measured isolation of around -17 dB is obtained between the two elements of the first array (elements 1 and 2). As for the isolation between element 2 of the first array and element 4 of the second array, the maximum value is almost -15 dB. The isolation levels are mainly set by the distance of separation between the elements as well as the position of the various elements. All these parameters have been optimized for best performance through simulations.

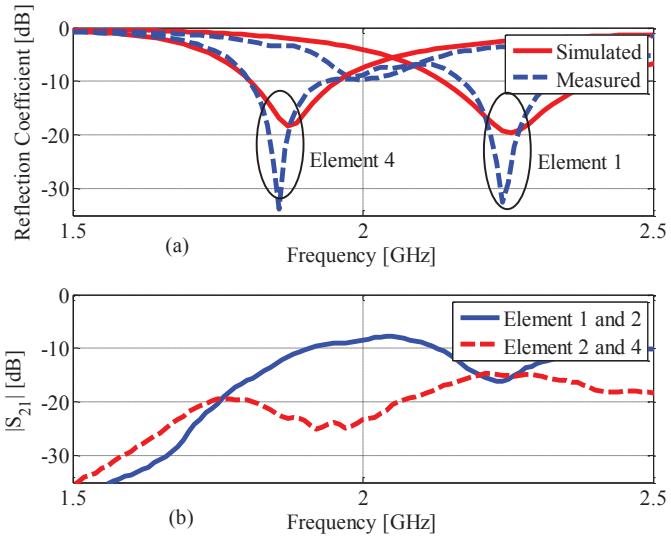

Figure 40. (a) The simulated and measured reflection coefficient for elements 1 and 4 of the two arrays, (b) The measured isolation between elements 1 and 2 as well as elements 2 and 4.

The reflection coefficient of the array is also further investigated under four different scenarios. The first scenario is related to the case when elements 1 and 2 of the first array are connected to a power splitter while the remaining two elements are terminated by 50 Ω. The reflection coefficient at the input of the splitter is shown in Figure 41a. The second scenario is similar to the first one but now the first two elements are loaded by 50 Ω and elements 3 and 4 are connected to the same power splitter. Figure 41a also highlights the reflection coefficient for the second scenario. From these two plots, one notices that reflection coefficients exhibit great similarities to the ones shown in Figure 40a. This is due to the good isolation between the various elements. In the third scenario, the four elements of the array are fed simultaneously where elements 1 and 2 are connected to one power splitter and elements 3 and 4 are connected to a second power splitter. Figure 41b presents the measured S-parameters between the two input ports of the splitters. One notices that the measured isolation between the two arrays is kept below -15 dB. The two arrays maintain the same operating bandwidth when they are both actively fed. A slight shift in the resonant frequency is noticed in comparison to the first scenario. The simulated results are also included in Figure 41b where a close agreement is noticed with the measured data. The simulated results are obtained by modeling each power splitter by its corresponding S-parameters matrix. This is achieved by relying on the S3P file supplied by the manufacturer. The two arrays can be represented as a four ports system. The modeling of such system using S4P S parameter file can be obtained from the electromagnetic simulator.

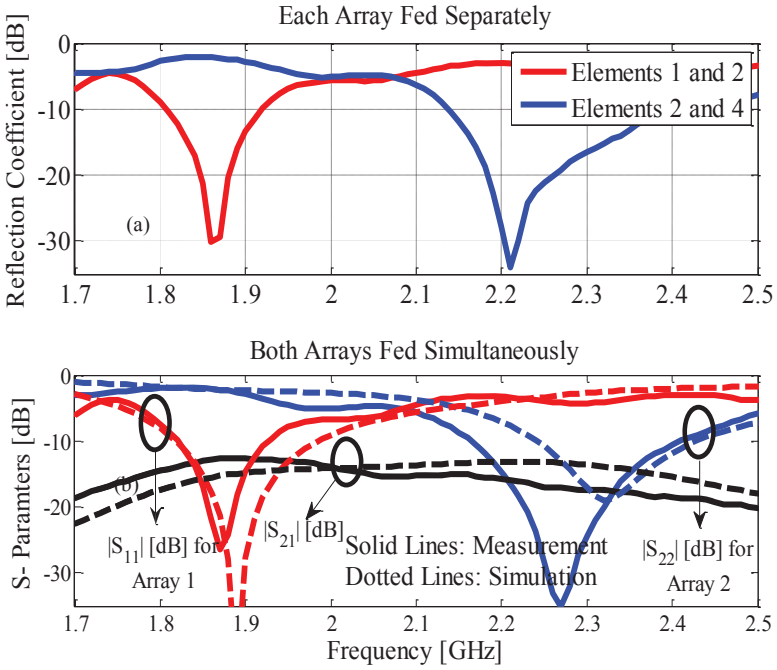

Figure 41. (a) The measured reflection coefficient when only one element either array is fed (scenario 1 and 2), (b) The comparison between the simulated and measured reflection coefficient when each array is fed by a power splitter simultaneously (scenario 3).

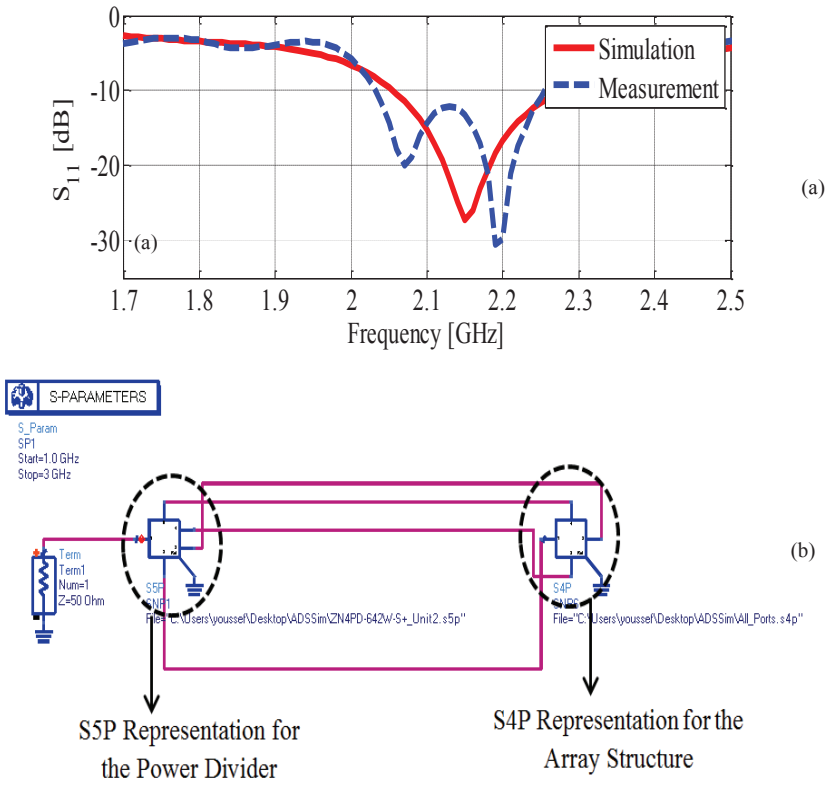

Figure 42. (a) The reflection coefficient for the case when the four elements are fed by a four ways power splitter (scenario 4), (b) The corresponding simulation setup for scenario (4).

In the last scenario, a one to four power splitter is used to feed all the four elements of the array. The simulated and measured reflection coefficients for this case are highlighted in Figure 42a. For this case, the operating bandwidth is narrower since the power splitter is feeding two different arrays that do not operate over the same span of frequencies. Figure 42b represents the simulation setup for this scenario where the splitter is modeled by its S5P file and the array by its corresponding S4P file.

In the first three scenarios, the ZN2PD-9G-S+ and ZAPD-2-272-S+ power splitters from mini-circuits [50, 51] were used while for the fourth scenario the ZN4PD-642W-S+ [52] was employed. Both power combiners exhibit low insertion low (≈ 0.5-1 dB) and a phase imbalance of less than 4º. Such phase imbalance between the different elements was accounted for in the simulation of the array where minimal effect as noticed on the impedance match as well as the total gain patterns for different frequencies. The transmission lines used in the experimental setup had equal lengths to guarantee a uniform phase shift and almost equal insertion loss.

The radiation patterns of each array were tested by loading the elements of the other array by 50 Ω. Figure 43a shows the comparison between the simulated and measured normalized radiation patterns at f=2.29 GHz for both Φ= 0º and Φ= 90º cut planes. The results of the

second array at *f*=1.87 GHz for both cut planes is highlighted in Figure 43b. The measured and simulated patterns show good agreement.

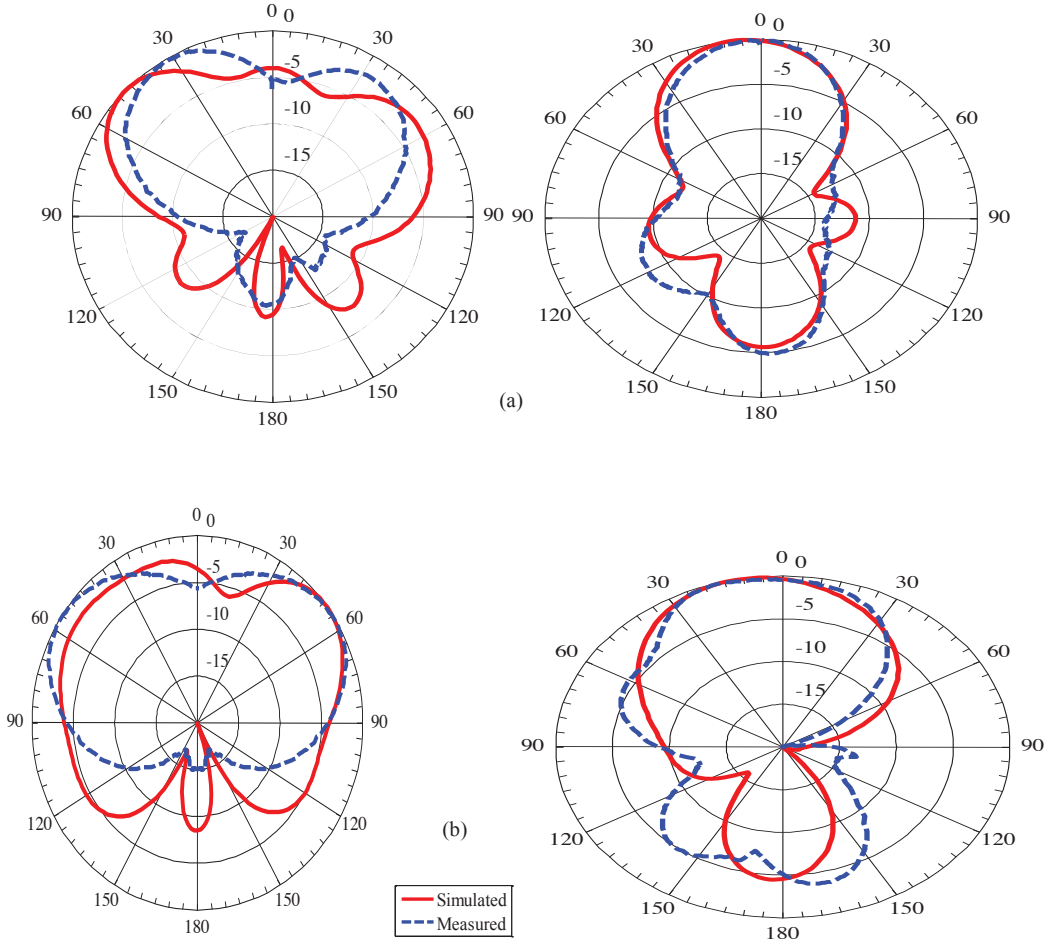

Figure 43. (a) The normalized array radiation pattern for Φ= 0° (left) and Φ= 90° (right) cut planes (a) for the first array at *f*=2.29 GHz, (b) and for the second array at *f*=1.87 GHz.

3.4.3 Effect of Antenna Arrays on the Solar Panel

The copper based array structures presented previously were positioned orthogonal to the upper and lower edges of the integrated solar panel. The purpose of the vertical positioning of the array elements was to reduce the possibility of sunlight blockage. In order to validate the positioning of the antenna arrays and to insure that the minimum blockage was occurring, two transparent antenna arrays were designed and positioned in the same manner as the copper based arrays. Evaluating the effect of the antennas on the solar panel's ability to harvest sunlight is essential to this design. This is due to our objective which was based on achieving an efficient dual source (EM/solar) of an energy harvesting system. It was important to insure that both systems are compatible and did not affect each other negatively.

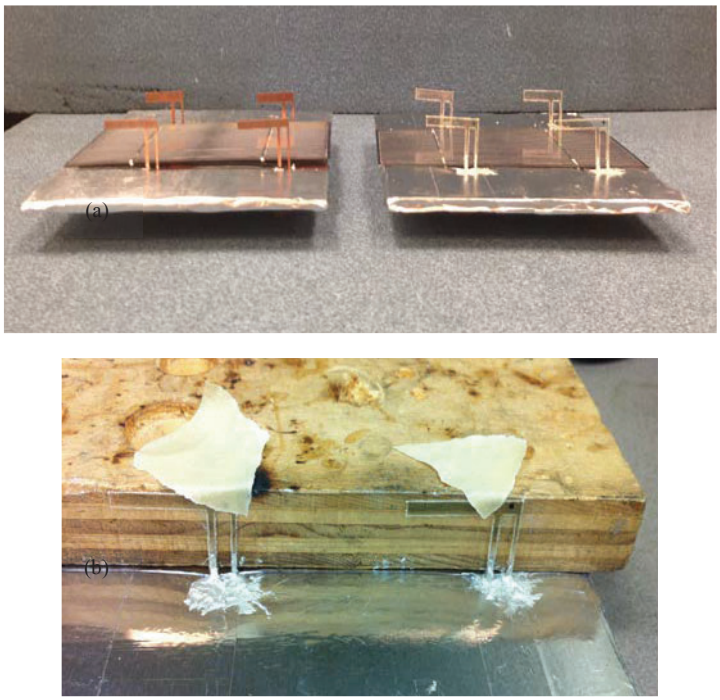

Figure 44. (a) The fabricated copper and transparent array structure with the solar panel, (b) The soldering setup of the transparent array elements where the conductive silver epoxy is apparent on the array ground plane.

Each transparent antenna structure was based on a transparent conductive oxide (TCO) polymer film that is AgHT-4 with a conductivity of $25x10^4$ (S/m) [53-56]. The most common technique when dealing with transparent material is to place the radiating structure parallel to the solar panel where the panel acts as the substrate for the antenna structure. However, in this work, the transparent inverted-F antenna elements had to be positioned along the same topology (vertical) of the copper based ones to insure the fidelity of our comparison analysis. In addition, in order to assess the effect of the copper based inverted-F antenna arrays on the performance of the solar panels same conditions must be reproduced for accurate evaluation.

The different transparent antenna arrays shared the same dimensions as the copper antenna arrays. Figure 44a highlights the fabricated copper (left side) and transparent (right side) arrays. The fabrication and testing process of the transparent antenna arrays was delicate. The appropriate soldering of each shorting arm of the various antenna elements to the ground plane as well as the soldering of each feeding arm to the SMA connector is critical to the operation of the proposed structure. The polymer film comes with a protective layer that must be carefully etched and removed to reach the conductive top layer of each antenna arm for soldering. Also, cold soldering techniques using conductive silver epoxy must be adopted. Such soldering technique requires resting the antennas for long hours, before completing the testing process, in order to ensure that good contact is maintained as shown in Figure 44b.

Figure 45 shows the simulated and measured reflection coefficient when both arrays were fed with two separate power splitters. This corresponds to scenario 3 discussed previously. The

transparent antenna arrays exhibited the same radiation pattern characteristics as the copper ones.

The effect of the transparent array on the solar panel was compared to the copper structure. Both arrays are placed simultaneously under sunlight and the measured voltage drawn by the solar cell is measured. The experiment was run from 11 am until 3 pm where the voltage was measured every 15 min. The average voltage for the transparent array was 0.578 V while for the copper array the average voltage was found to be 0.562 V. Based on this experiment, it was confirmed that the placement of the copper elements in an orthogonal fashion at both edges of the panel has a minimal effect on the solar energy efficiency. It is preferred to integrate copper elements due to their higher conductivity levels. Also, transparent materials such as AgHT-4 are very expensive and require lot of effort to appropriately route the RF signal to the conductive layer.

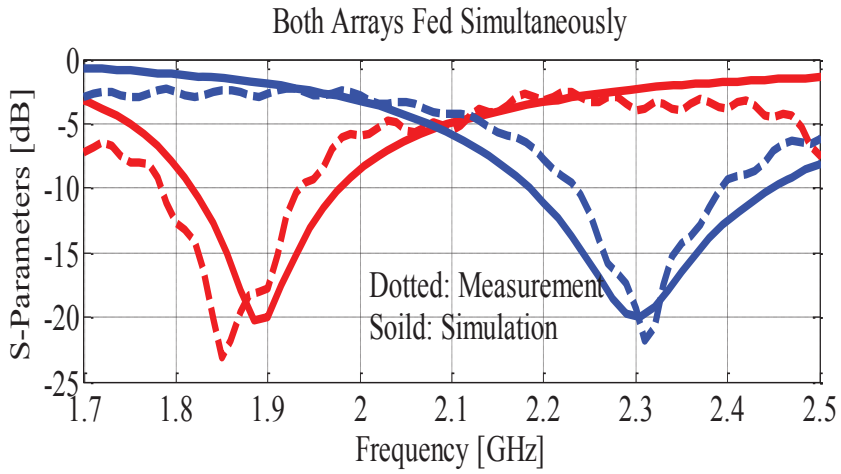

Figure 45. The reflection coefficient for the transparent array when both arrays are fed simultaneously through two different power splitters (scenario 3).

3.4.4 Rectifier Circuit Design

The final stage of this work was based on designing a rectifying circuit that was connected to the copper based radiating structure discussed previously. The copper based array structure was used since it achieves similar effect on the solar panel as the transparent one. The integration of copper elements is preferred over transparent in case the array is scaled to be incorporated into bigger solar panels.

The next step was to decide whether a single rectifier was sufficient to be connected to the two arrays simultaneously or a separate rectifying circuit must be used for each array. Having one rectifying circuit to feed the input port of the 1-to-four power splitter (scenario 4) is not recommended since under this case the array produces narrower. Thus, the decision was made to design a wideband rectifying circuit that operates over the whole bandwidth from 1.8 GHz

up till 2.4 GHz. The wideband feature is essential to enable the same rectifying circuit to feed each array separately by connecting it to the 1-to 2 power splitter (scenario 3). The DC outputs from both rectifiers and the solar panel can be either combined or used separately to supply three different sources of power. The DC power combination can be achieved using a DC power management circuit such as the one implemented in [57].

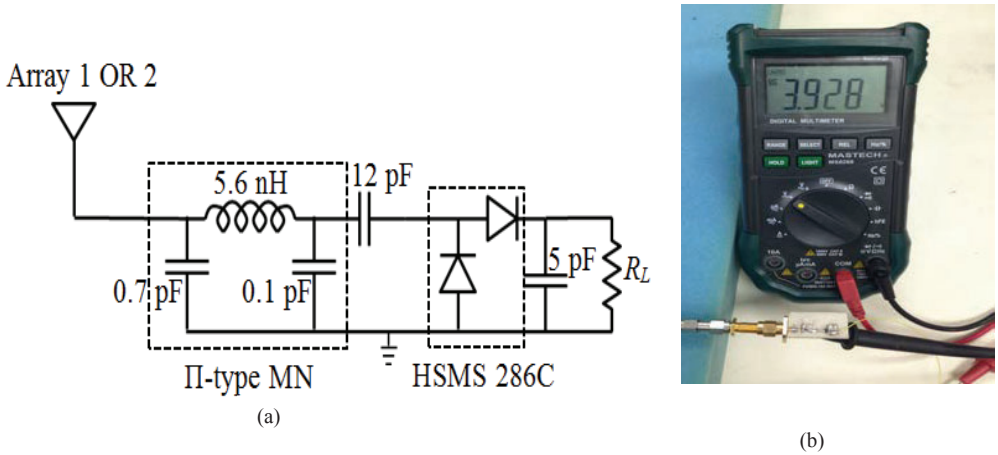

Figure 46. (a) The structure of the voltage doubler rectifying circuit, (b) The corresponding fabricated prototype.

Figure 46a presents the structure of the designed rectifier circuit. The wideband behavior was achieved by designing a π-type matching network with a quality factor of 2. A voltage doubler topology was adopted by relying on the HSMS-286 Schottky diode configuration. Such configuration provides two diodes connected in a series-parallel manner in one component [57]. The load resistance was optimized to be 1 KΩ to guarantee good performance for different power levels at the input of the wideband matching network. The rectifying circuits that fed the two arrays did not affect the performance of the solar panel and neither the antenna array since they were placed underneath the ground plane of the whole system. The fabricated rectifying circuit is shown in Figure 46b. The rectifying circuit was able to maintain a good performance for the span of frequencies between 1.4 GHz and 2.4 GHz.

Figure 47a presents the measured rectification efficiency for three different frequencies. The data in this plot corresponds to the case where the rectifier is tested without being connected to the antenna array. The next step was to feed the rectifier to the antenna array. Figure 47b shows the corresponding rectenna efficiency at the resonant operating frequency of the two arrays (1.87 GHz and 2.29 GHz). The incorporation of the π-type matching network enables the same rectifier to be used for both arrays.

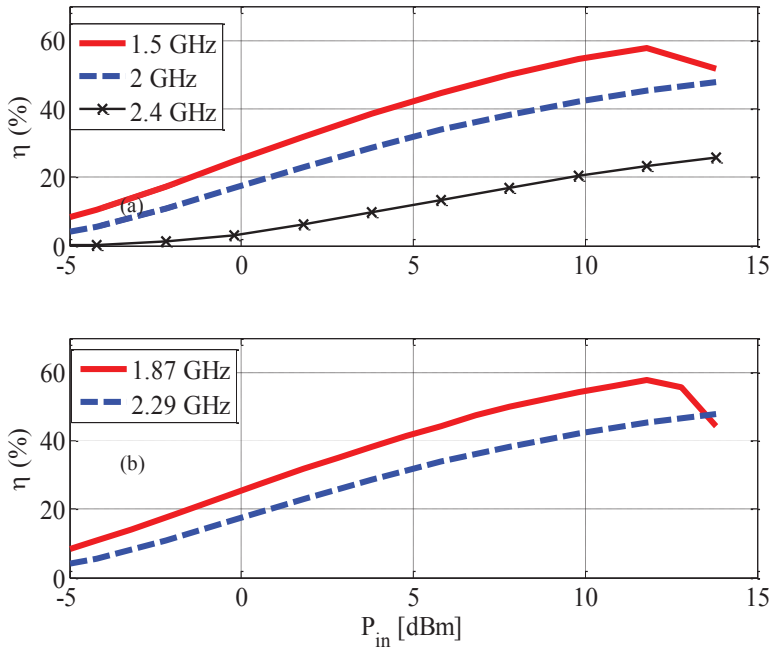

Figure 47. (a) The measured efficiency of the wideband rectifier circuit, (b) The rectification efficiency at the resonant frequency of the two arrays.

In general, the orthogonal placement of the various elements of the array at the upper and lower edge of the panel was proven to have a minimal effect on the solar panel efficiency. The DC output of the rectenna systems and solar panel can be combined to result in a diverse dual source energy harvesting solution.

3.5 Ridge-fed Conical Horn Antenna

Next, a foldable conical horn antenna for high gain, wideband cubesat applications was developed. The ridge-fed conical horn antenna designed is shown in Figure 48. The horn aperture was chosen to achieve a minimum gain of 10 dB at the lowest frequency and maintain that over the desired frequency range. The feed and design parameters were adjusted to allow for the added capacitance due to the horn shroud. The feed points were optimized and simulated using CST Microwave Studio. A coarse mesh grid was selected to increase the computational accuracy. The port impedance was set to 75Ω for matching purposes.

Figure 49 shows the reflection coefficient from the antenna input which shows a good transition at 75Ω over the entire frequency of interest. There is a shift at higher frequencies which is expected due to the capacitance added by the integration of the horn structure and the

coupling between the fields of the radiating structures (Vivaldi radiators) inside the conical horn.

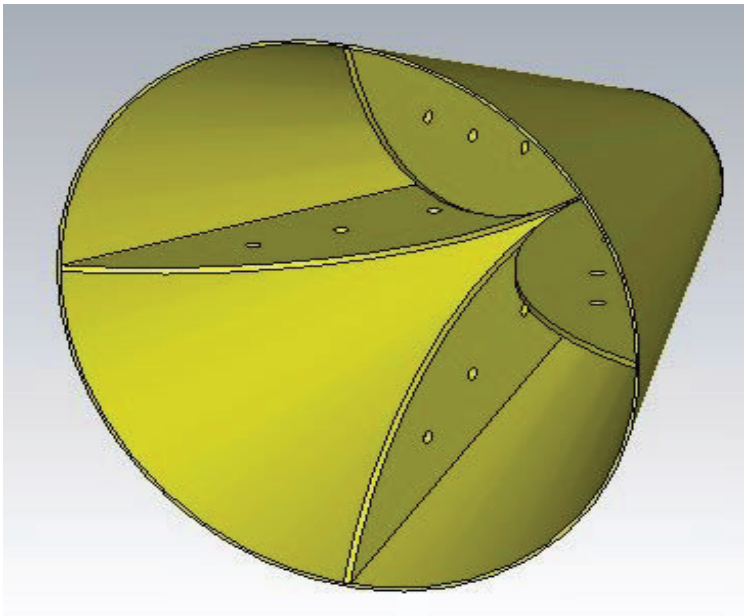

Figure 48. Concept: Ridge-fed conical horn antenna.

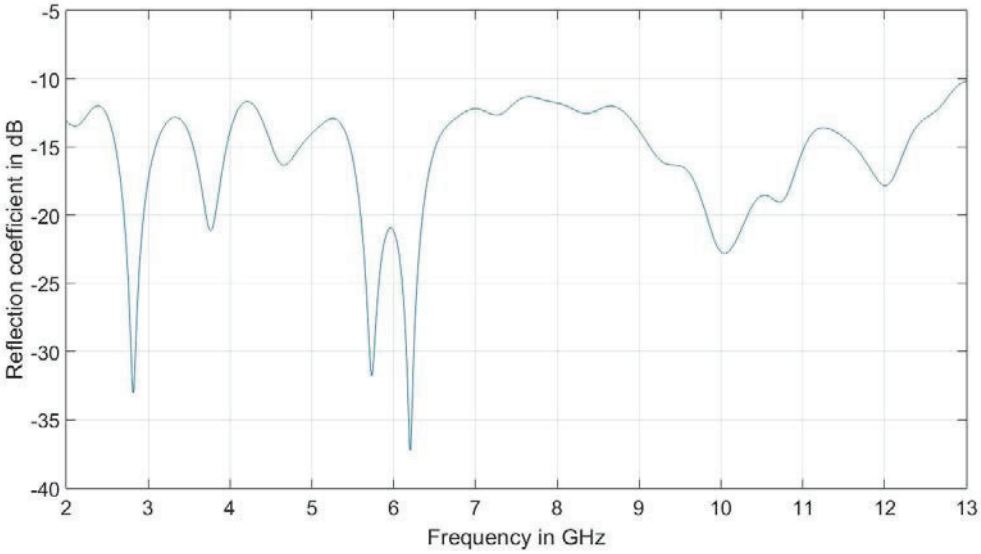

Figure 49. Reflection Coefficient Ridge-fed Conical Horn antenna.

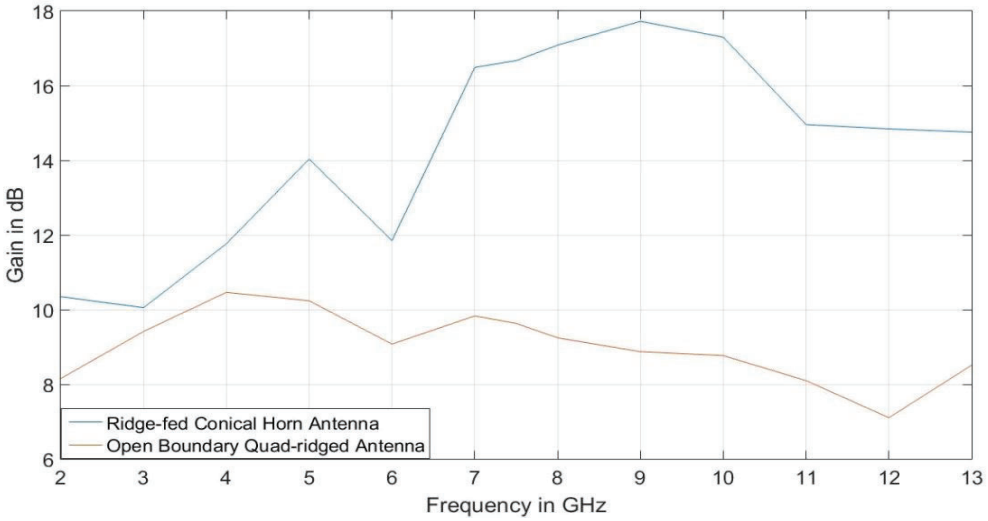

Figure 50. Discretized gain plot of the Ridge-fed Conical Horn antenna compared with the gain of the Quad-ridged horn antenna.

After ensuring a smooth transition, the next step was to look for the radiation and how well the antenna was matched to free space. The gain of the antenna is plotted against frequency in Figure 50 which meets the gain requirement for the design. The gain of the Quad-ridged (without the conical enclosure) is also plotted as a comparison.

The horn structure drives a higher gain but it does affect its beam width as shown in Figure 51. The increase in gain by an order of magnitude resulted in a considerable decrease in the beam width as predicted. This is a classical trade-off associated with antennas in general, more so in horn antennas [58,59]. Typically, in high frequency transmission systems a directive source is required to compensate for the losses.

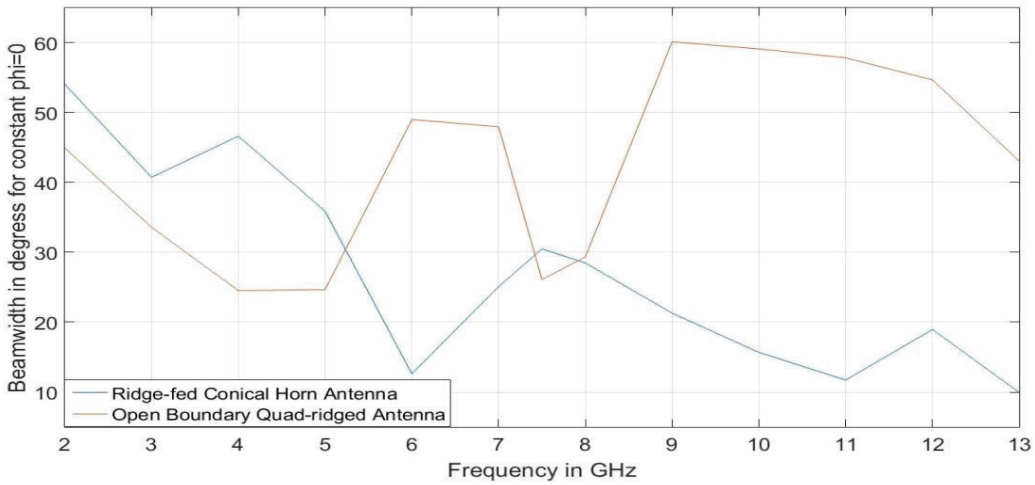

Figure 51: Angular 3dB beam width of the Ridge-fed Conical Horn antenna com- pared with the Quad-ridged and plotted against frequency.

The next figure of merit for the designed antenna was the axial ratio, since circular polarization is critical for operation in most cubesat applications. The axial ratio at boresight is plotted against frequency in Figure 52. The entire band is circularly polarized except at 12 GHz where it jumps to 3.0416 dB which is not exactly desired but optimization can be done to bring that down below the threshold of 3dB. The incorporation of the horn changed the radiation patterns of the simple Quad-ridged antenna (Vivaldi radiators without the conical enclosure).

The radiation patterns for 2 GHz to 7 GHz is plotted in dB in Figures 53a and 53b. The antenna exhibits nicely formed main lobes for the lower frequencies with 2 GHz having the highest beamwidth which gradually decreases as the gain increases. The beam gets directive with frequency and takes the shape of a pencil beam as theorized. At 6 GHz, there was substantial destructive interference and required further optimization.

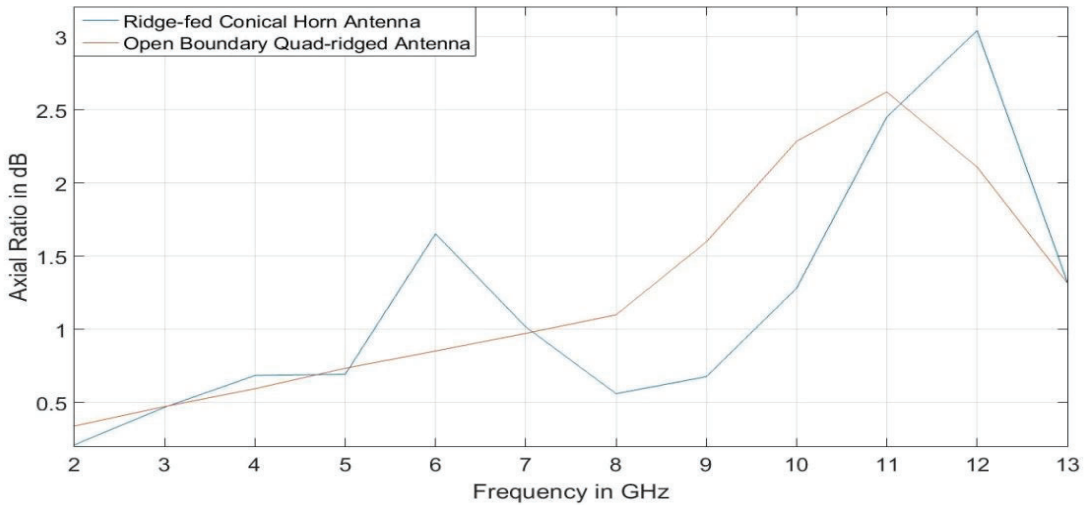

Figure 52: Axial Ratio in dB at boresight of the Ridge-fed Conical Horn antenna compared with the Quad-ridged and plotted against frequency.

The patterns for 8 GHz, 9 GHz and 10 GHz, shown in Figure 54, are almost identical with a single pencil beam achieving a high directivity and gain and an angular beam width of about 18◦. The pattern deteriorates again at 12 GHz which is a multiple of 6 GHz, which can be purely co-incidental or might be the destructive interference for the wavelength and its multiples. The antenna radiates at boresight for the entire band except at 12GHz where the main beam splits in to two, which is common in wideband horn antennas covering over a decade of impedance matched bandwidth [59].

Thus, a wide band antenna with most of the desired attributes set out to achieve was designed and evaluated. Next, the fabrication and measurement process of the antenna to prove the functionality of the design are described.

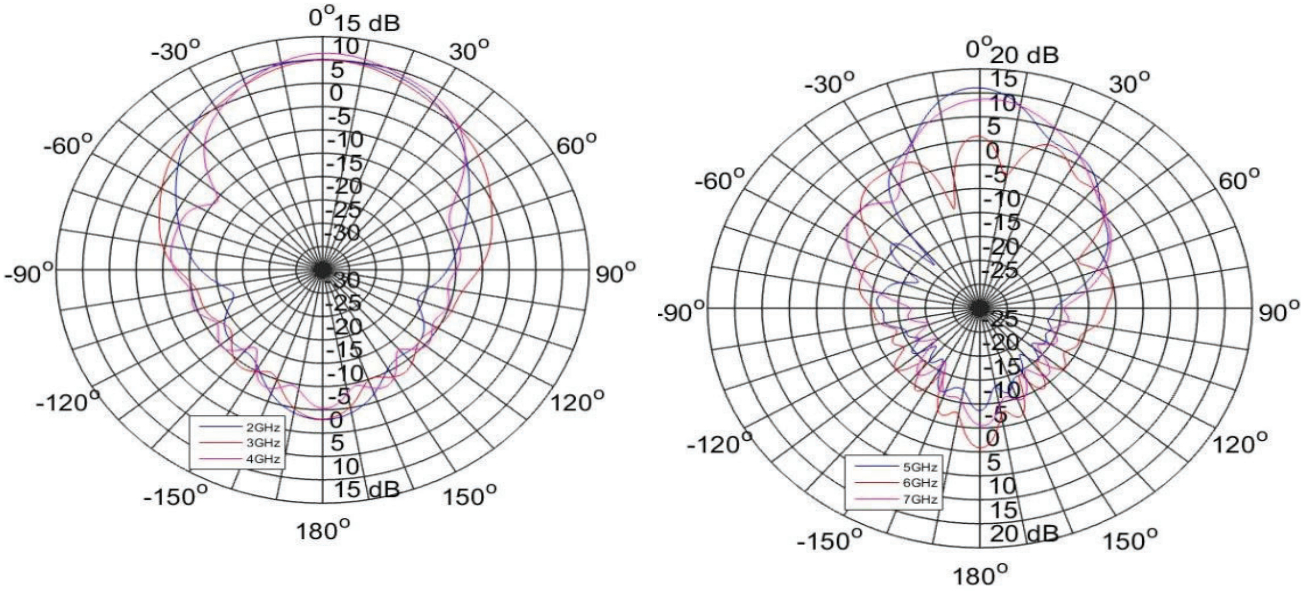

Figure 53. (a) Radiation Pattern at 2GHz, 3GHz, and 4GHz. (b) Radiation Pattern at 5GHz, 6GHz, and 7GHz.

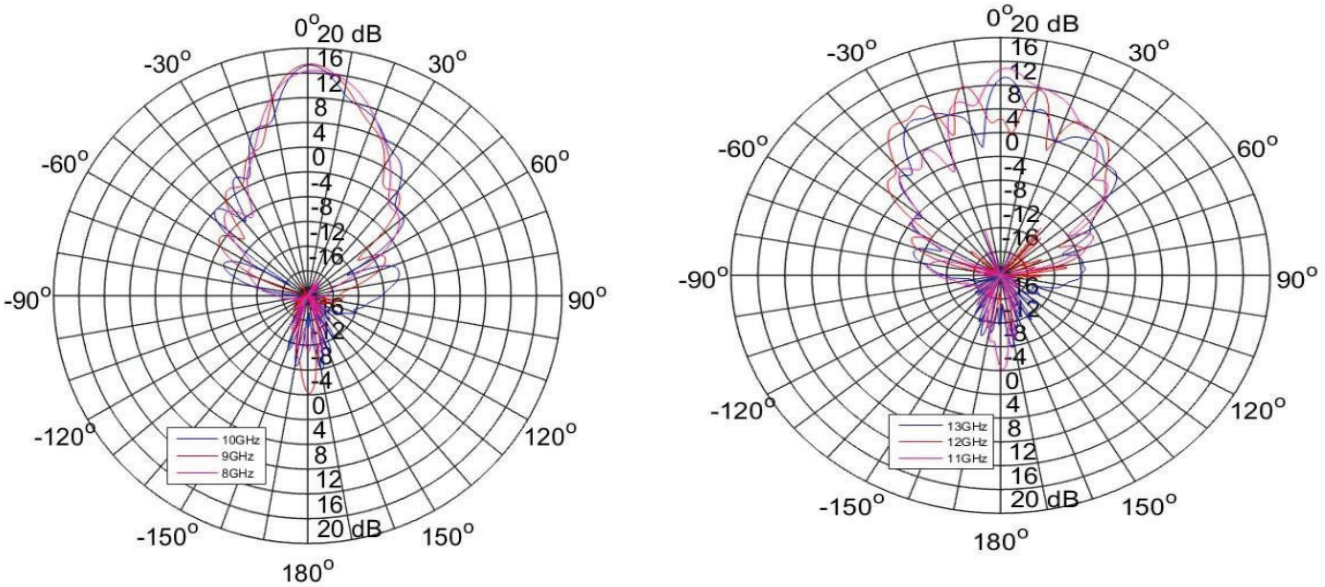

Figure 54. (a) Radiation Pattern at 8 GHz, 9 GHz, and 10 GHz. (b) Radiation Pattern at 11GHz, 12 GHz and 13 GHz.

3.5.1 Antenna Fabrication & Measurement

The first prototype was fabricated on copper to prove the fidelity of the design but copper is too heavy and rigid for practical deployment mechanisms. A new material was subsequently investigated to make the design light weight and robust for autonomous deployment.

3.5.1.1 Prototype

The prototype was fabricated on a 2mm copper plate to match the simulations. The quad ridged antenna was fabricated on copper plate using a Computer Numeric Control (CNC) machine. The design for each fin was extracted from CST microwave studio in a dxf format which is readable by any AutoCAD software used for mechanical fabrications. The two fin shapes were cut out from a copper slab and the feed point was marked as shown in Figure 55 below.

Figure 55. Fabricated fin

After the fin fabrication the feed slot was cut on one side of each fin to insert the probe and feed the fin at an optimized location just below the ridges. The feed slot was carefully shaped in a milling machine, a fraction of a mm at a time until the desired and simulated feed slot was achieved to fit to insert the probe.

Once the feed slot was perfected the probe was inserted through the slot on the arm to feed the optimized feed point below the ridge on the adjacent arm of the fin. The same

procedure was repeated with the other fin and the two fins were soldered and integrated together to form
the quad-ridged open boundary horn antenna. For simplicity in the feeding structure the coax was stripped to the dielectric and the outer conductor was grounded on the arm holding the feed (the other arm of the feed fin). The inner conductor needs to be carefully soldered, keeping in mind the margin for error is 0.2mm since the feed overlaps with each other over such a small gap. A coax probe with a very small inner conductor diameter is recommended and preferred for this application. The details of the above mentioned steps are shown in Figure 56.

Figure 56. (a)Feed slot milled on the fin side (b) Inserted coax which turns into a probe and feeds the ridge.

The fabrication of the feed is of extreme importance and needs high precision instruments to insert the feed and solder it to the optimal feed point.

3.5.1.2 Measurement and Results

The antenna system designed required a 75Ω test bench which was unavailable and hence the antenna was tested on a 50Ω test bench and the results were analyzed and compared to a 50Ω simulation done on the same structure. The first figure of merit obtained was the S-parameters. The measurement was done with a single port calibrated and connected to the input of a commercial phase shifter from RFLambda which has a frequency bandwidth of 2-18GHz with minimized loss as shown in Figure 57.

The measured data shows a clear viable bandwidth (See Figure 58) over the entire spectrum, whereas the antenna was actually matched to a 75Ω. This was largely due to the fact that

there was a loss associated with the coupler and the cable, which in this case was equal to -2.4dB, combined at the highest operating frequency. If that is taken into account the plot will look very close to the simulated one for 50Ω. There is also an error associated with fabricating the optimized feed at the exact locations and the shape of the structure due to the numerous experiments performed on it.

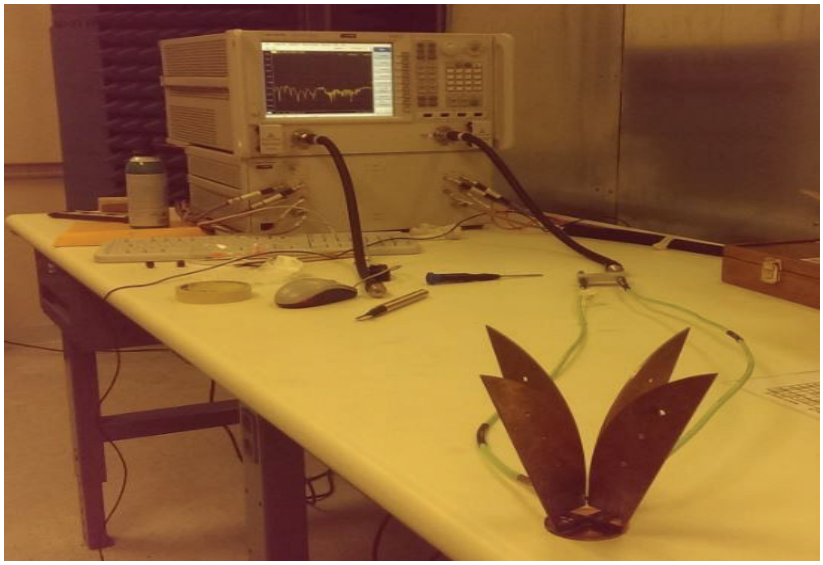

Figure 57. S-parameter measurement set up for the fabricated quad-ridge.

The next figure of merit was the gain of the antenna. The antenna gain was measured in the anechoic chamber over a standard sectoral horn antenna from AH systems. The gain was calculated from the power received by the standard horn antenna using a gain transfer method [4].

The power received from the AUT (Antenna Under Test) was measured first which is subsequently replaced by a standard horn antenna and the power level is measured again under the same conditions. The Gain of the AUT then, is given by the equation 1.

$$G_{AUT} = G_s + 10\log_{10}(\frac{P_T}{P_s}) \quad (1)$$

Where,

G_{AUT} = Gain of antenna under test.

G_S = Gain of the standard horn antenna.
P_T = Power received from test antenna.
P_S = Power received from standard horn.

There is an amount of power lost due to the transmission lines, insertion loss of the cables and the phase shifter. The loss is classified with respect to frequency by manufacturer, that loss is

added to the gain to get the absolute gain value. Since the antenna is circularly polarized, the power transmitted in the horizontal and vertical plane were measured separately and then the absolute gain of the antenna is given by the equation 2.

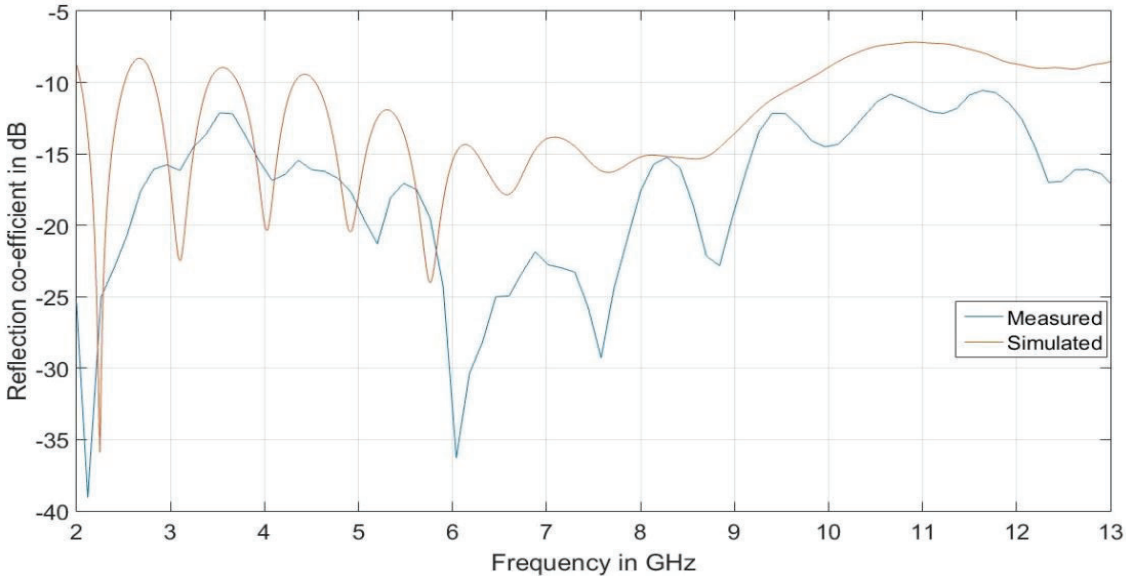

Figure 58. Γ comparison between measured and simulated for 50Ω.

$$G_{AUT}(dB) = 10\log_{10}(G_{TV} + G_{TH}) \quad (2)$$

Since the antenna was operational between 5 GHz and 9 GHz due to a 50Ω test bench, the gain was calculated for only four frequencies and is tabulated below.

Table 5 . Measured and Simulated gain results.

Frequency (GHz)	Measured Gain (dB)	Simulated Gain (dB)
5	6.94	10.1
6	7.89	7.04
7	7.54	7.53
8	6.39	6.54

The gain values matched well with the simulations except for at 5GHz where it is significantly less which was attributed to the fabrication tolerance of the feed structure.

The measured patterns at 2 GHz, 3 GHz, 7 GHz, and 13 GHz for both Vertical and Horizontal planes of the antenna are plotted against the simulated results to demonstrate the

radiation characteristics of the designed antenna in Figures 59 through 62. The lower frequencies seem to match better with the simulation than their higher counterpart. As mentioned earlier the fabrication error is high in the prototypes but the radiation patterns for both planes follow the pattern of the simulations if not match exactly.

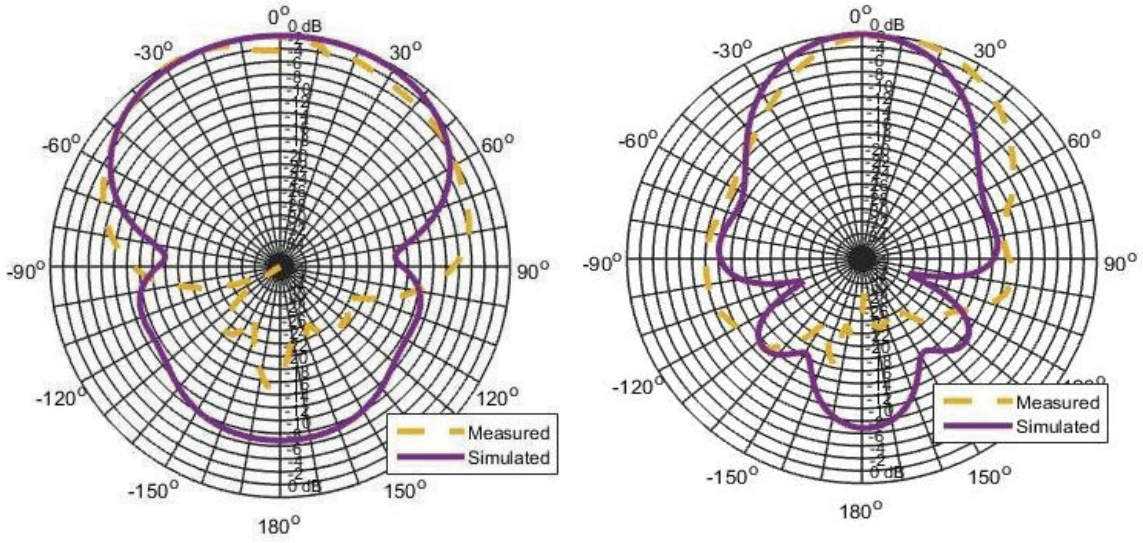

Figure 59. (a) 2 GHz radiation pattern horizontal plane. (b) 2GHz radiation pattern vertical plane.

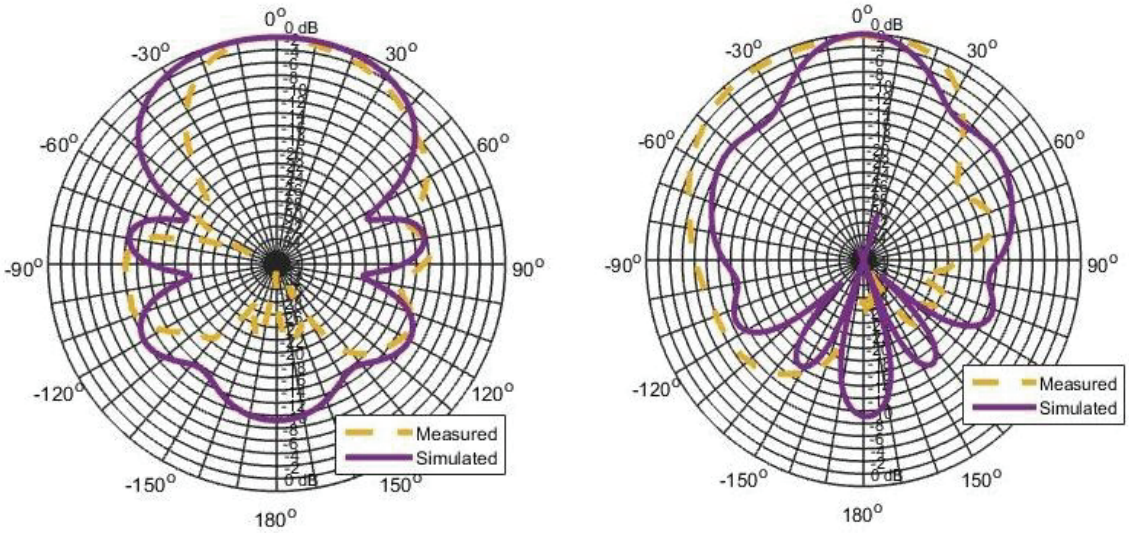

Figure 60. (a) 3GHz Horizontal radiation pattern. (b) 3GHz Vertical radiation pattern.

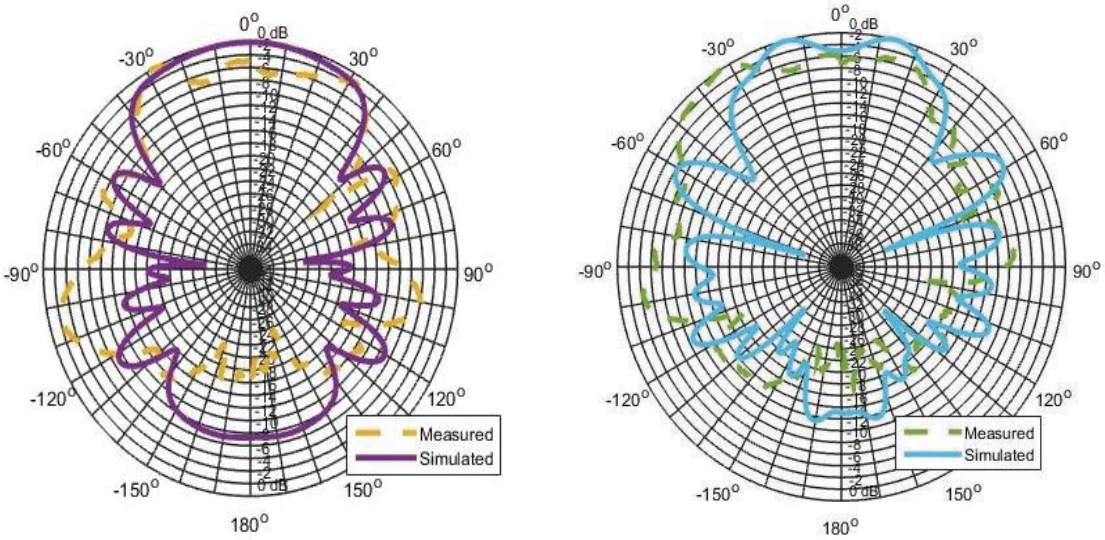

Figure 61. (a) 7 GHz Horizontal radiation pattern. (b) 7GHz Vertical radiation pattern

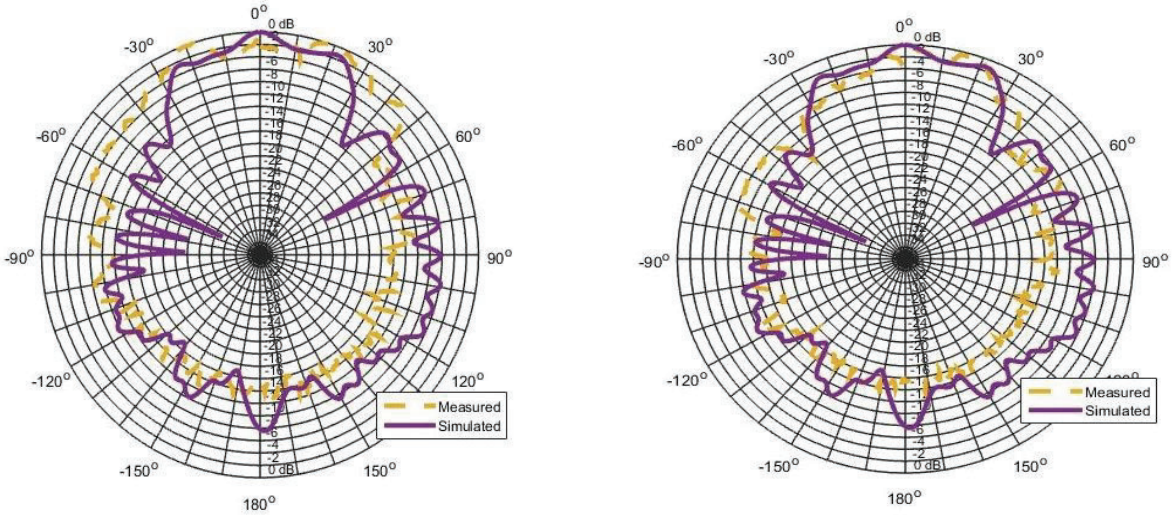

Figure 62. (a)13GHz Horizontal radiation pattern. (b) 13GHz Vertical radiation pattern.

3.5.2 Material Characterization

Some of our collaborator at AFRL and Caltech came up with a composite structure made up of highly conductive mesh which would make the antenna light weight, yet act as a conductor and minimize skin depth for the frequency spectrum and ensure proper radiation. The composite structure is composed of Phosphor bronze mesh (35µm wire diameter and 325 wires/inch), Astroquartz fabric, Carbon fiber plain weave, epoxy film and conductive epoxy tape. These layers were stacked up in different combinations to create the optimum combination. The categories for each of these materials are given in Figure 63 below to better understand the composite.

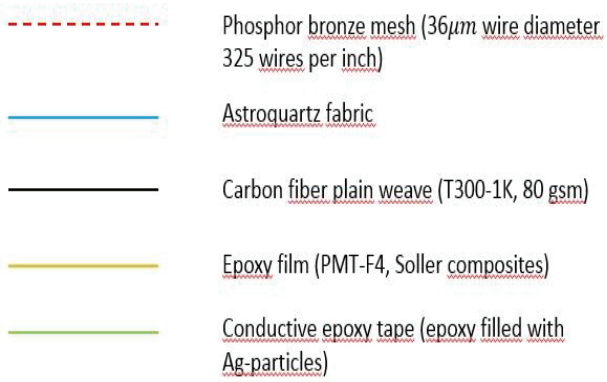

Figure 63: Material Description

The first two materials were atroquatrz fiber based structures. The fiber was treated with epoxy film and the mesh on the top. The sample in Figure 64a was infiltrated and covered with a thin film of non-conductive epoxy while that in 64b was covered with conductive epoxy. This material fabrication was done by Prof. Pellegrino's group at Caltech and tested at UNM.

Substrates 3,4,5 and 6 were based on carbon fiber with fibers running in orthogonal directions are shown in Figures 65 and 66. The substrates are made up of highly conductive mesh comparable to that of copper. The overall conductivity of the four substrates which were not coated with the non-conductive epoxy was found to be in the orders of 10^7S/m which is comparable to the conductivity of copper at $5.8*10^7$S/m. Electrically, the high conductivity establishes the viability of these substrates and vindicates the phosphor bronze mesh epoxy composite as a good and light weight alternative for conventional antenna materials which can be deployed from a small satellite platform. Further research should include fabrication of the designed structure to specification and testing the deployment mechanism and the antenna performance after the structure has been deployed. A material

study needs to be performed to study the effects of space radiation and outgassing on the composite structure.

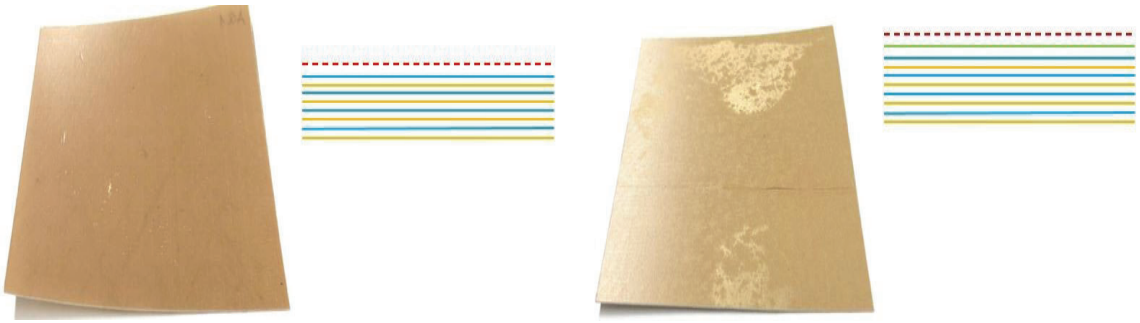

Figure 64. (a) Substrate 1. (b) Substrate 2.

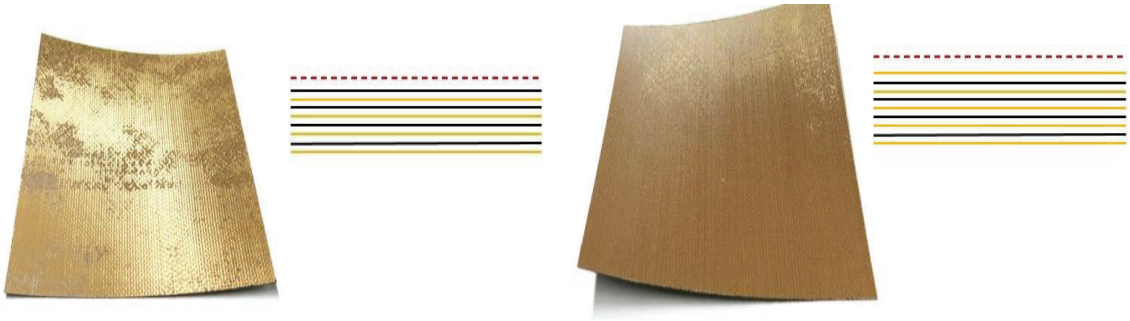

Figure 65. (a) Substrate 3. (b) Substrate 4.

Figure 66. (a) Substrate 5. (b) Substrate 6.

4 CONCLUSION

The design, analysis, and implementation of several antenna architectures for cubesats were presented in details. The design characteristics and applications of each suitable antenna candidate are thoroughly discussed and their suitability for deployment is emphasized.

Potential deployable composite tape spring antenna concepts were proposed for CubeSat applications. These antennas exhibit good bandwidth, circular polarization and a satisfactory gain.

The proposed bi-stable glass composite tape spring with imbedded copper alloy conductive element introduces new possible antenna configurations for CubeSats. Next, conventional horn design techniques were modified to facilitate the deployment of a ridge fed conical horn antenna. The design which included the use of a new material can lead to the development of light weight and sturdy, deployable, and wideband horn antennas.

In addition, an antenna system that is composed of different sets of curved and straight dipoles was discussed. The integration of a printed parasitic curved reflector was implemented to further improve the radiation characteristics of the various elements. The proposed system featured good diversity for both structures in various propagation environments. Reconfigurable feeding networks were also incorporated within the antenna system to control which radiating structure is excited.

Finally, an antenna architecture that can be used on cubesats for both communication and RF harvesting purposes was included. Two antenna arrays were integrated vertically on top of a solar panel, from opposite edges for RF harvesting purposes, on top of solar harvesting. Copper based inverted-F antennas constituted the elements of both antenna arrays. Also, two transparent antenna arrays, of same physical dimensions and topologies as the copper ones, were also investigated. The goal was to validate the integration of the copper based inverted-F antenna arrays on top of the solar panel. A rectifying circuit that was positioned at the output of both arrays was also designed and tested. The measured performance results of the fabricated prototypes for the two arrays as well as the rectifying circuit showed good agreement with the simulated data.

5 REFERENCES

1. Muri, P., Obulpathi, C., and McNair, J., "Enhancing Small Satellite Communication Through Effective Antenna System Design," *2010 Military Communications Conference – Unclassified Program,* San Jose, CA, 2010.
2. Gao, S., Clark, K., Unwin, M., Zackrisson, J., Shiroma, W.A., Akagi, J.M., Maynard, K., Garner, P., Boccia, L., Amendola, G., Massa, G., Underwood, C., Brenchley, M., Pointer, M., and Sweeting, M.N., "Antennas for modern small satellites," *IEEE Antennas and Propagation Magazine*," Vol. 51, No. 4, pp. 40–56, 2009.
3. Rahamat Samii, Y., and Densmore, A.C., "Technology Trends and Challenges of Antennas for Satellite Communication Systems," *IEEE Transactions on Antennas and Propagation*," Vol. 63, no.4, pp.1191-1204, 2015.
4. Kitsuregawa, T., **Advanced Technology in Satellite Communication Antennas**, Artech House, Norwood, MA, 1990, p. 299.
5. Fujishige T., "Active Antennas for CubeSat Applications," *16th AIAA/USU Conference on Small Satellites*, 2002.
6. Costantine, J., Tawk, Y., Moth, S., Christodoulou, C.G., and Barbin, S.E., "A Modified Helical Shaped Deployable Antenna for Cubesats," *IEEE APWC'12*, Cape Town, South Africa, pp. 1114-1116, 2012,
7. Costantine, J., Tawk, Y., Maqueda, I., Sakovsky, M., Pellegrino, S., and Christodoulou, C.G., "UHF Deployable Helical Antennas for CubeSats," *IEEE Transactions on Antennas and Propagation*, pp. 3752-3759, 2016.
8. Kakoyiannis, C. G., and Constantinou P., "A compact microstrip antenna with tapered peripheral slits for CubeSat RF Payloads at 436MHz: Miniaturization techniques, design & numerical results," *Proceedings of the IEEE International Workshop on Satellite and Space Communications (IWSSC 2008),* pp. 255–259, 2008.
9. Milligan , T., **Modern Antenna Design**, Wiley-IEEE Press, 2nd Edition, 2005.
10. Costantine, J., Tawk, Y., Ernest, A., and Christodoulou, C.G., "Deployable Antennas for CubeSat and Space Communications," *6th European Conference on Antennas and Propagation,* 2012.
11. Dyson, J., "The Characteristics and Design of the Conical Log-Spiral Antenna," *IEEE Transactions on Antennas and Propagation*, Vol. 13, pp 488-499, 1965.
12. Murphey, T. W., and Pellegrino, S., "A Novel Actuated Composite Tape-Spring for Deployable Structures", *Tech. Rep., AIAA, TR-1528*, 2004.
13. Murphey, T. W., Jeon, S., Biskner, A., and Sanford,G., "Deployable Booms and Antennas Using Bi-stable Tape-springs," *24th AIAA/USU Conference on Small Satellites*, Logan, Utah, 2010.
14. Murphey, T.W., Jeon, S., Biskner, A., and Sanford, G., "Deployable Booms and Antennas Using Bi-stable Tape-springs," *24th AIAA/USU Conference on Small Satellites*, Logan, Utah, 2010.
15. Jeon, S., and Murphey, T.W., "Design and analysis of a meter-class CubeSat boom with a motor-less deployment by bi-stable tape springs," *52nd AIAA Structures, Structural Dynamics, and Materials Conference,* pp. 4-7. 2011.
16. http://jpsglass.com/.

17. Balanis, C.A., **Antenna Theory Analysis and Design**, John Wiley and Sons, third edition, 2005.
18. Chen, S., and Luk, K.M., "A dual-mode wideband MIMO cube antenna with magneto-electric dipoles," *IEEE Transactions on Antennas and Propagation*, Vol. 62, No. 12, pp. 5951-5959, 2014.
19. Lin , W., and Wong, H., "Polarization reconfigurable wheel-shaped antenna with conical-beam radiation pattern," *IEEE Transactions on Antennas and Propagation*, Vol. 63, no. 2, pp. 491-499, 2015.
20. Gu, C., *et al*., "Compact smart antenna with electronic beam-switching and reconfigurable polarizations," *IEEE Transactions on Antennas and Propagation*, Vol. 63, No. 12, pp. 5325-5333, 2015.
21. Wu, B. Q., and Luk, K.M., "A 4-port diversity antenna with high isolation for mobile communications," *IEEE Transactions on Antennas and Propagation*, Vol. 59, No. 5, pp. 1660-1667, 2011.
22. Oh, J., and Sarabandi, S., "Compact, low profile, common aperture polarization, and pattern diversity antennas," *IEEE Transactions on Antennas and Propagation*, vol. 62, no. 2, pp. 569-576, Feb. 2014.
23. Qin, Z., Geyi, W., Zhang, M., and Wang, J., "Printed eight-element MIMO system for compact and thin 5G mobile handest," *Electronics Letters*, Vol. 52, No. 6, pp. 416-418, 2016.
24. Li, M.Y., *et al*., "Eight-port orthogonally dual-polarized antenna array for 5G smartphone applications," *IEEE Transactions on Antennas and Propagation*, Vol. 64, No. 9, pp. 3820-3830, 2016.
25. Ban, Y. L., Li, C., Sim, C.Y.D., Wu, G., and Wong, K.L., "4G/5G multiple antennas for future multi-mode smartphone applications," *IEEE Access*, Vol. 4, No. , pp. 2981-2988, 2016.
26. Anitha, R.,Vinesh, P.V., Prakash, K.C., Mohanan , P., and Vasudevan, K., "A compact quad element slotted ground wideband antenna for MIMO applications," *IEEE Transactions on Antennas and Propagation*, Vol. 64, No. 10, pp. 4550-4553, 2016.
27. Ramachandran, A., Valiyaveettil Pushpakaran, S., Pezholil, M., and Kesavath, V., "A four-port MIMO antenna using concentric square-ring Patches Loaded With CSRR for High Isolation," *IEEE Antennas and Wireless Propagation Letters*, Vol. 15, No. , pp. 1196-1199, 2016.
28. Sarkar, D., Singh, A., Saurav, K., and Srivastava, K. V., "Four-element quad-band multiple-input–multiple-output antenna employing split-ring resonator and inter-digital capacitor," *IET Microwaves, Antennas and Propagation*, vol. 9, no. 13, pp. 1453-1460, 10 22 2015.
29. Tawk, Y., Costantine, J., Ramadan, A. H., Kabalan, K. Y., and Christodoulou, C.G., "A reconfigurable feeding network," *The 8th European Conference on Antennas and Propagation,* The Hague, pp. 1534-1536, 2014.
30. Tawk, Y., Christodoulou, C.G., and Costantine, J., "An integrated two MIMO antenna system based on directive printed dipoles," *IEEE International Symposium on Antennas and Propagation & USNC/URSI,* pp. 705-706, 2015.
31. TDK Corporation (Part number: HHM1732B1), http://www.tdk.com .
32. Balanis, C. A., **Modern Antenna Handbook**, John *Wiley & Sons*, 2008.
33. Sharawi, M.S., **Printed MIMO Antenna Engineering**, Artech House, Norwood, MA, 2014.

34. Taga, T., "Analysis for mean effective gain of mobile antennas in land mobile radio environments," *IEEE Transactions on Vehicular Technology*, Vol. 39, No. 2, pp. 117-131, 1990.
35. Knudsen, M. B., and Pedersen, G. F., "Spherical outdoor to indoor power spectrum model at the mobile terminal," *IEEE Journal on Selected Areas in Communications*, Vol. 20, No. 6, pp. 1156-1169, 2002.
36. Blaunstein, N., Christodoulou, C.G.,and Sergeev, M. B., "Capacity and Weight Coefficients in MIMO Wireless Communication Channels Based on Adaptive Multi-beam Antennas in Urban Environment with Fading", in Информационно-управляющие системы, No. 6, pp. 107-117, 2014.
37. Diallo, A., Luxey, C., Le Thuc, P., Staraj, R., and Kossiavas, G., "Diversity performance of multiantenna systems for UMTS cellular phones in different propagation environments," *International Journal of Antennas and Propagation*, Vol. 2008, 2008.
38. Moghaddam, S. M., Glazunov, A. A., Kildal, P. S., Yang, Y., and Gustafsson, M., "Improvement of an Octave Bandwidth Bowtie Antenna Design Based on the Analysis of a MIMO Efficiency Metric in Random-LOS," *Microwave and Optical Technology Letters*, Vol. 59, No. 6, 2017.
39. Carlberg, U., Carlsson, J., HussainA., and Kildal, P. S., "Ray based multipath simulation tool for studying convergence and estimating ergodic capacity and diversity gain for antennas with given far-field functions," 2*0th International Conference on Applied Electromagnetics and Communications*, pp. 1-4, 2010.
40. Kildal, P.S., Orlenius, C., and Carlsson, J., "OTA testing in multipath of antennas and wireless devices with MIMO and OFDM," *Proceedings of the IEEE*, Vol. 100, No. 7, pp. 2145-2157, 2012.
41. Kildal, P. S., and Carlsson, J., "New approach to OTA testing: RIMP and pure-LOS reference environments & a hypothesis," *7th European Conference on Antennas and Propagation (EuCAP)*, pp. 315-318, 2013.
42. Infineon Technologies (Part number: BAR64-02V), http://www.infineon.com.
43. Yin, J., Nyberg, D., Xiaoming Chen, and Kildal, P. S., "Characterization of multi-port eleven antenna for use in MIMO system," *IEEE International Symposium on Wireless Communication Systems*, pp. 473-477, 2008.
44. Palaniswamy, S. K., Selvam, Y. P., Alsath, M.G.N., Kanagasabai, M., Kingsly, S., and Subbaraj, S., "3-D Eight-Port Ultrawideband Antenna Array for Diversity Applications," *IEEE Antennas and Wireless Propagation Letters*, Vol. 16, pp. 569-572, 2017.
45. Popovic, Z., Korhummel, S., Dunbar, S., Scheeler, R., Dolgov, A., Zane, R., Falkenstein, E., and Hagerty, J., "Scalable RF energy harvesting," *IEEE Transactions on Microwave Theory and Techniques*," vol. 62, No. 4, pp. 1046-1056, 2014.
46. Niotaki, N., Collado, A., Georgiadis, A., Kim, A., and Tentzeris, M. M., "Solar Electromagnetic energy harvesting and wireless power transmission," *Proceedings of the IEEE*, Vol. 102, No. 11, pp. 1712-1722, 2014.
47. Peter, T., Rahman, T. A., Cheung, S. W., Nilavalan, R., Abutarbouch, H. F., and Vilches, A., "A novel transparent UWB antenna for photovoltaic solar panel integration and RF energy harvesting," *IEEE Transactions on Antennas and Propagation,* Vol. 62, No. 4, pp. 1844-1853, 2014.

6 LIST OF SYMBOLS, ABBREVIATIONS, AND ACRONYMS

AUT	Antenna Under Test
Balun	Balance to Unbalanced Tranformer
DG	Diversity Gain
DG_{MRC}	Combining Diversity Gain
Cubesat	Cube sized Small Satellite
HPBW	Half Power Beamwidth
ITO	Indium Tin Oxide
LOS	Line of Sight
MEG	Mean Effective Gain
MIMO	Multiple Input Multiple Output
NEM	Neutrally Elastic Mechanism
RIMP	Rich Isotropic Multipath Propagation
TARC	Total Active Reflection Coefficient
TCO	Transparent Conductive Oxide